Remote Sens. **2015**, *7*, 3153-3183; doi:10.3390/rs70303153

OPEN ACCESS

remote sensing

ISSN 2072-4292

www.mdpi.com/journal/remotesensing

Article

Toward Estimating Wetland Water Level Changes Based on Hydrological Sensitivity Analysis of PALSAR Backscattering Coefficients over Different Vegetation Fields

Ting Yuan [1,2], Hyongki Lee [1,2,*] and Hahn Chul Jung [3,4]

[1] Department of Civil and Environmental Engineering, University of Houston, N107 Engineering Building 1, Houston, TX 77204, USA; E-Mail: tyuan@uh.edu

[2] National Center for Airborne Laser Mapping, University of Houston, 5000 Gulf Freeway Building 4 Room 216, Houston, TX 77204, USA

[3] Office of Applied Sciences, NASA Goddard Space Flight Center, 8800 Greenbelt Road, Greenbelt, MD 20771, USA; E-Mail: hahnchul.jung@nasa.gov

[4] Science Systems and Applications, Inc. (SSAI), 10210 Greenbelt Road, Lanham, MD 20706, USA

* Author to whom correspondence should be addressed; E-Mail: hlee@uh.edu; Tel.: +1-713-743-4685; Fax: +1-713-743-0186.

Academic Editors: Guy J.-P. Schumann and Prasad S. Thenkabail

Received: 13 January 2015 / Accepted: 9 March 2015 / Published: 19 March 2015

Abstract: Synthetic Aperture Radar (SAR) has been successfully used to map wetland's inundation extents and types of vegetation based on the fact that the SAR backscatter signal from the wetland is mainly controlled by the wetland vegetation type and water level changes. This study describes the relation between L-band PALSAR σ_0 and seasonal water level changes obtained from Envisat altimetry over the island of Île Mbamou in the Congo Basin where two distinctly different vegetation types are found. We found positive correlations between σ_0 and water level changes over the forested southern Île Mbamou whereas both positive and negative correlations were observed over the non-forested northern Île Mbamou depending on the amount of water level increase. Based on the analysis of σ_0 sensitivity, we found that denser vegetation canopy leads to less sensitive σ_0 variation with respect to the water level changes regardless of forested or non-forested canopy. Furthermore, we attempted to estimate water level changes which were then compared with the Envisat altimetry and InSAR results. Our results demonstrated a potential to generate two-dimensional maps of water level changes over the wetlands, and thus may have substantial synergy with the planned Surface Water and Ocean Topography (SWOT) mission.

Keywords: SAR; radar altimetry; water level changes; SWOT

1. Introduction

Tropical wetlands are one of the most important sources of global carbon and methane emissions, and play a significant role in regulating water balance and maintaining biodiversity [1–3]. Hydrologic conditions are extremely important for the maintenance of a wetland's structure and function [4]. The Congo Basin in Africa is the third largest basin in terms of its size (~3.7 million km^2), and second only to the Amazon River in discharge (~40,200 $m^3 \cdot s^{-1}$ annual average). However, only few studies have focused on its hydrology and hydrodynamics due to limited *in situ* data resulting from its historical political instability and poor civil infrastructure. Over the past few years, remote sensing became a viable tool to investigate Congo's terrestrial water dynamics and fluvial processes with Interferometric Synthetic Aperture Radar (InSAR) [5], satellite-derived precipitation datasets [6], satellite radar altimetry and the Gravity Recovery and Climate Experiment (GRACE) data [7].

The capability of InSAR to explore the hydrologic changes in wetlands was first demonstrated by [8] using L-band HH-polarized SIR-C data over the Amazon floodplain, and further utilized to spatially map the passage of a flood wave from the Amazon floodplain using L-band JERS-1 data [9]. Later, Wdowinski *et al.* [10] also used the JERS-1 SAR data to study the water level changes over the Everglades wetlands in Florida. Besides the L-band SAR data, Lu and Kwoun [11] found that interferograms generated with C-band Radarsat-1 and ERS SAR data can also maintain adequate coherence under medium-low canopy closure over the Louisiana swamp forests. The advantage of this InSAR technique is that it provides highly accurate (centimetric) water level changes over the vegetated wetlands with high spatial resolution (usually 10~30 m). However, there exist several shortfalls as well. Firstly, a coherent SAR pair, constrained by temporal and spatial baselines and surface scattering characteristics, is required to generate the interferogram [12]. Secondly, the interferograms may only be generated over the wetlands with stable trunks of vegetation (e.g., swamp forests) [8,10,11] or structures [13] which enable the reflected radar signal to follow the double-bounce travel path. Finally, the interferograms generated from InSAR can only provide a spatially relative gradient of water level changes. Vertical reference data is needed to convert the relative changes into absolute changes [13,14].

Apart from InSAR which utilizes interferometric phase differences between two SAR scenes, SAR backscattering coefficient (σ_0) has been widely used to classify flooded and non-flooded areas with their vegetation types based on the fact that hydrological changes over wetlands can result in variations in SAR backscattering coefficients [15,16]. Accordingly, there have been efforts to quantify the relation between hydrologic conditions and σ_0 using theoretical scattering models. For example, Kasischke *et al.* [17] tried to correlate C-band ERS-2 σ_0 with regional hydrologic changes, vegetation types, and biomass in the Everglades wetlands of Florida. They found that the ERS-2 σ_0 is closely related to both soil moisture and water level changes in the Marl Prairie sites which seasonally experience complete dry condition. Later, Grings *et al.* [18,19] used C-band Envisat ASAR scenes and electromagnetic models with field work data to examine SAR backscatter responses to water level changes over marshes of the Parana River Delta. In addition, Trung *et al.* [20] studied changes in land cover classes in the Tonle Sap

floodplain using PALSAR and MODIS data with a land cover model as a function of water level. Recently, Kim *et al.* [21] has investigated relationships between L-band PALSAR σ_0 and water level changes from *in situ* gauge over the Everglades freshwater marshes. The relations were then used to estimate a reference water level change to convert relative water level changes obtained from PALSAR interferograms to absolute water level changes. However, the Everglades may be the only wetland in the world equipped with a dense network of water gauges installed for its restoration project, while most of the wetlands in the world lack cost-prohibitive *in situ* water gauges.

Alternatively, satellite radar altimetry has been successfully used to monitor water level changes over rivers, lakes, and wetlands [22,23]. For example, Envisat altimetry [7] has been used to highlight the hydrodynamic differences between the Congo wetlands and the Amazon floodplains. Although satellite altimetry is a nadir-looking one-dimensional profiling instrument and thus needs an intersection with a water body, it is currently the only remote sensing instrument that can provide periodic water level changes from space [24]. In this study, we used the wetland water level changes obtained from Envisat altimetry instead of *in situ* data to investigate its relationship with the L-band PALSAR σ_0. In addition, because the radar backscattering mechanism depends on vegetation types as well, the Vegetation Continuous Field (VCF) [25,26] product derived from the Moderate Resolution Imaging Spectroradiometer (MODIS) was used to investigate the PALSAR backscattering sensitivity to different vegetation fields under hydrologic changes. Finally, we attempted to estimate wetland water level changes based on the relationship between backscattering sensitivity to water level changes and VCF data, which were compared with water level changes obtained from InSAR and Envisat altimetry.

2. Study Area

The Congo River is the largest river in Africa with a large number of islands. The largest number of channels and islands are found in the Malebo Pool, located upstream of the Livingstone Fall. The Malebo Pool is surrounded by extensive palms and papyrus swamps along the edges and floating mats of Eichhornia frequently pass through [27]. The annual amplitude of water level change in the Malebo Pool is about 3 m, and water flows quickly towards the ensuing Livingstone Fall with an average flow of 30,000 $m^3 \cdot s^{-1}$ and 60,000 $m^3 \cdot s^{-1}$ in flooding time [28]. The biggest island in the Malebo Pool is called the Île Mbamou, which is our study area (Figure 1). It separates the Congo River into two channels, and most of the water flow through the channel south of the Île Mbamou to the Livingstone Fall.

Figure 1a shows the 3-arcsecond resolution C-band Shuttle Radar Topography Mission (SRTM) Digital Elevation Model (DEM) over our study region. Interestingly, we observe that the SRTM DEM values are distinctly different over the southern and northern parts of the Île Mbamou. Since this SRTM DEM is generated with C-band (5.6 cm wavelength) SAR data which cannot penetrate vegetation canopy [11,29], the measured scattering phase center is usually above bare ground and lower than tree height [30]. Consequently, the SRTM elevations are biased upward above the ground into the tree canopy, and not representing the bare-earth topography. Therefore, it is likely that the higher SRTM DEM values over the southern island partly represent its higher canopy height. It is consistent with the land cover map shown in Figure 1b from the GLCNMO (Global Land Cover by National Mapping Organizations) 2008 [31]. The southern part of the Île Mbamou is dominated by "broadleaf evergreen forest" while the northern part of the Île Mbamou is occupied by "herbaceous vegetation" and "open

canopy". However, an old French literature found in [32] indicates that the topography between the southern and northern parts of the island may be indeed different.

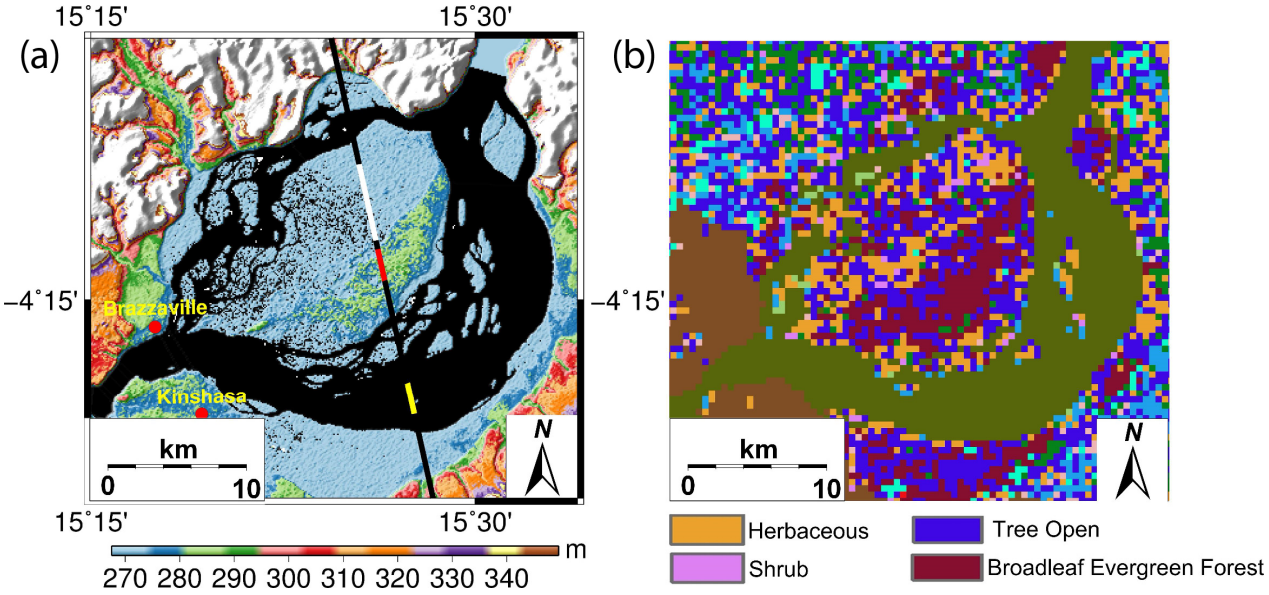

Figure 1. (**a**) Envisat's pass 143 (black line) over our study area. The central island represents the Île Mbamou. Background is the C-band SRTM DEM; (**b**) Land cover map from GLCNMO2008 [31].

3. Data Sets

3.1. Envisat Radar Altimetry

In this study, we used Envisat RA2 Geophysical Data Record (GDR) of pass 143, from the period of October 2002 (cycle 10) to September 2010 (cycle 93). The ascending pass 143 flies over the Malebo Pool from south to north, sequentially intersecting the southern reach of the Congo River, the Île Mbamou, and northern reach of the Congo River (Figure 1a). The Envisat RA2 GDR contains 18-Hz (~350 m along-track sampling) retracked range observations using OCEAN, ICE-1, ICE-2, and SEA ICE retrackers. Among these, we chose the ICE-1 retracker [33]. The instrument corrections, media corrections (dry and wet troposphere corrections from the European Centre for Medium-Range Weather Forecasts model, and the ionosphere correction based on Global Ionosphere Maps), and geophysical corrections (solid Earth and pole tides) were applied. In addition, the 5.6 m level Ultra Stable Oscillator (USO) anomalies for cycles 44–85 were corrected using the European Space Agency's correction table.

3.2. PALSAR Backscattering Coefficients

We used fourteen ALOS PALSAR images obtained at ascending direction with a look angle of 34.3°, spanning from June 2007 to February 2011, as listed in Table 1. Seven of them were obtained with Fine Beam Single (FBS) mode (HH polarization) while the other seven were obtained with Fine Beam Dual (FBD) mode (both HH and HV polarizations) [34,35]. We adopted images with HH polarization mode because it is known to be more sensitive to water level changes beneath vegetation [35,36] and provides better interferometric coherence [14]. We processed all PALSAR raw data to obtain single look complex

(SLC) images. It is noted that different bandwidths of FBD and FBS data lead to different ground range resolutions, *i.e.*, 28 MHz for FBS data and 14 MHz for FBD data [37]. To obtain consistent resolutions, the FBD images were oversampled by a factor 2 in the range direction. The SLC images were then co-registered to a common SLC image obtained on 13 December 2008. To reduce the effects of radar speckle noises, we applied a 4 × 9 multi-look factor to all of the SLC images. As a result, the spatial resolution of the multi-looked mages becomes approximately 30 m × 30 m. The backscattering coefficient (σ_0) can be computed with absolute calibration factors such as:

$$\sigma_0 = 10\log_{10}(DN^2) + CF \text{ (dB)} \quad (1)$$

where *DN* is the digital number of the intensity image, and *CF* is the radiometric calibration factor (−51.9 dB for FBS HH data, and −51.8 dB for FBD HH data) [38]. A median filter with 3 × 3 window was also applied to further reduce speckle noises. Since the topography is quite smooth over the study area, gamma naught (γ_0: σ_0 divided by the cosine of the incidence angle) is not considered in this study. Finally, all the σ_0 images were geocoded using 3-arcsecond SRTM DEM oversampled to 1-arcsecond resolution. However, it is noted that 1-arcsec SRTM DEM over Africa is now freely available [39].

Table 1. List of PALSAR scenes used this study.

Scene ID	Operation Mode	Date	Path	Frame	Polarization Mode
ALPSRP073347100	FBD	10 June 2007	607	7100	HV/HH
ALPSRP086767100	FBD	10 September 2007	607	7100	HV/HH
ALPSRP093477100	FBS	26 October 2007	607	7100	HH
ALPSRP100187100	FBS	11 December 2007	607	7100	HH
ALPSRP127027100	FBD	12 June 2008	607	7100	HV/HH
ALPSRP153867100	FBS	13 December 2008	607	7100	HH
ALPSRP180707100	FBD	15 June 2009	607	7100	HV/HH
ALPSRP194127100	FBD	15 September 2009	607	7100	HV/HH
ALPSRP207547100	FBS	16 December 2009	607	7100	HH
ALPSRP214257100	FBS	31 January 2010	607	7100	HH
ALPSRP234387100	FBD	18 June 2010	607	7100	HV/HH
ALPSRP247807100	FBD	18 September 2010	607	7100	HV/HH
ALPSRP261227100	FBS	19 December 2010	607	7100	HH
ALPSRP267937100	FBS	3 February 2011	607	7100	HH

3.3. MODIS VCF

The MODIS 250 m VCF collection 5 product was used in this study to represent the spatial heterogeneity of vegetation in the Île Mbamou. The VCF product is derived from all seven bands of the MODIS data [25,26]. It contains proportional estimates for vegetative cover types, including woody vegetation, herbaceous vegetation and bare ground, and thus is useful to show how much of a land cover such as "forest" or "grassland" exists [26]. The VCF data is available from 2000 to 2010, and we calculated mean VCF value from them which is shown in Figure 2. We can observe a clear difference in VCF over the northern (10%–20%) and southern (50%–70%) parts of the island. It indicates that the northern part is mostly covered with non-forest areas whereas forest is dominant over the southern part.

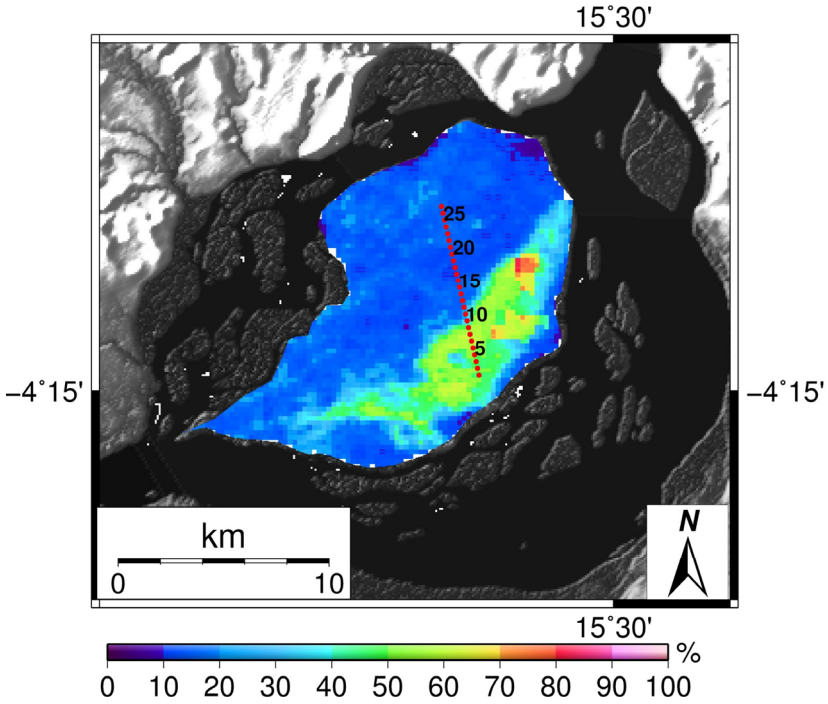

Figure 2. Map of MODIS VCF averaged using VCF data from 2000 to 2010 over the Île Mbamou. Envisat 18-Hz nominal footprints with their numbers are also plotted which are referred in Section 5.2.

After all, distinctly different vegetation types over the northern and southern parts of the island, along with the intersecting Envisat track make the Île Mbamou an ideal domain to test a regression model toward estimating water level changes based on σ_0 changes and MODIS VCF. Hereinafter, the northern Île Mbamou refers to the non-forested areas and the southern Île Mbamou refers to the forested areas.

4. Envisat Altimetry and Interferometric SAR Data Processing

4.1. Water Level Changes from Envisat Altimetry over the Malebo Pool

Typically, several high-rate (e.g., 18-Hz in case of Envisat altimetry) measurements obtained over intersections of satellite track and water bodies (river, lake, reservoir, wetlands) are spatially averaged to generate water level change time series. Figure 3 illustrates the surface height profiles along Envisat pass 143 obtained from several Envisat cycles over the Malebo Pool. We can observe fluctuations in the water levels over the southern Congo reach, and southern and northern parts of the Île Mbamou (marked with "1", "2", and "3", respectively, in Figure 3). We then generated water level change time series by combining successive overpasses. Figure 4a shows the time series over the southern reach of the Congo River using multiple 18-Hz Envisat altimetry measurements ("1" in Figure 3). After editing out spurious data, we observe its overall good agreement with daily *in situ* gauge data obtained at Brazzaville (Figure 1a) with a root-mean-square error (RMSE) of 34.9 cm and correlation coefficient of 0.95 using the daily *in situ* measurements temporally closest (black dots) to the Envisat altimetry measurements (Figure 4a). Part of the RMSE would be due to the fact that Brazzaville is located where the northern and southern Congo River meet, which resulted in higher amplitude of *in situ* time series. Similarly, we generated water level change time series by spatially averaging several 18-Hz Envisat altimetry

measurements over the southern and northern parts of the Île Mbamou ("2" and "3" in Figure 3, respectively), which both revealed 2–3 m of distinct seasonal variations (Figure 4b). Interestingly, we also observe from Figure 4b that the water over the forested area stays for a longer period of time than the water over the non-forested area (roughly 3 or 4 months), which may indicate that the forested land has a longer residence time.

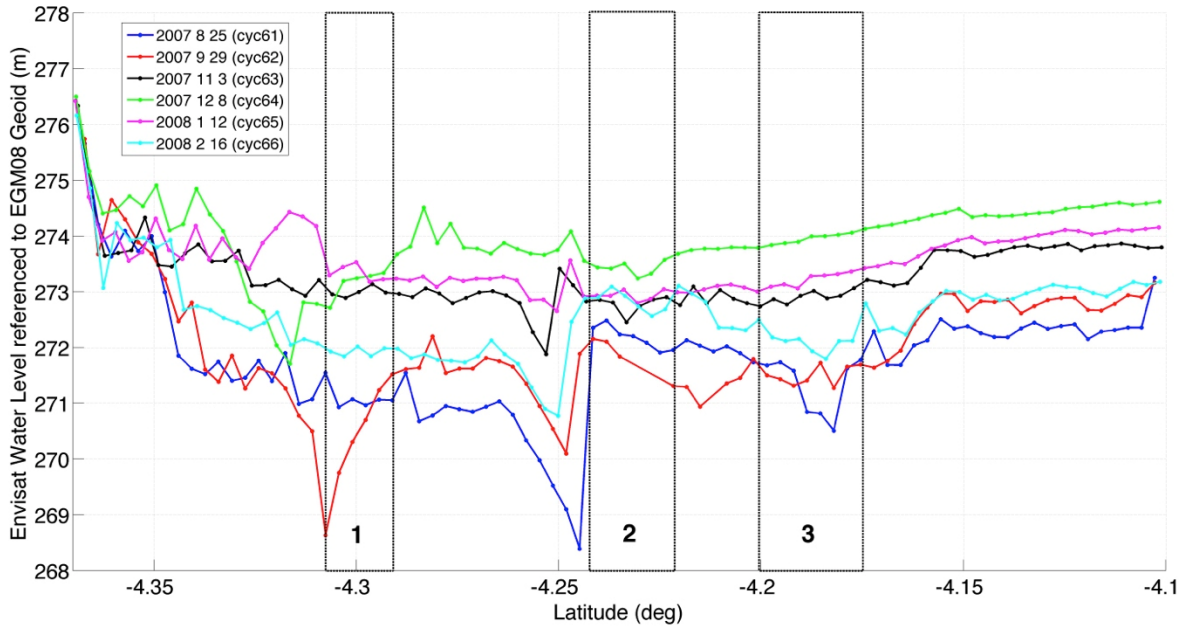

Figure 3. Water level fluctuations referenced to EGM08 geoid over the Île Mbamou along Envisat pass 143. The regions "1", "2", and "3" indicate the southern Congo River, the southern part of the Île Mbamou, and the northern part of the Île Mbamou, respectively. The yellow, red, and white colors along the pass in Figure 1 represent areas "1", "2", "3" shown above.

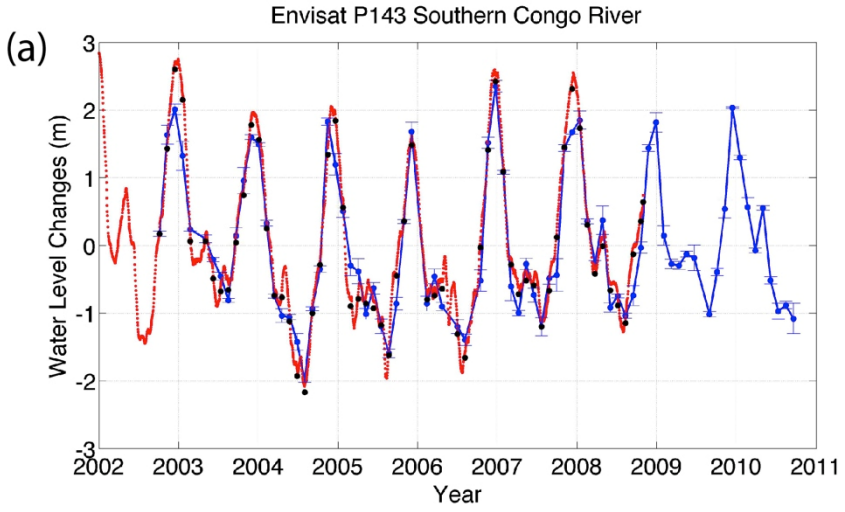

Figure 4. *Cont.*

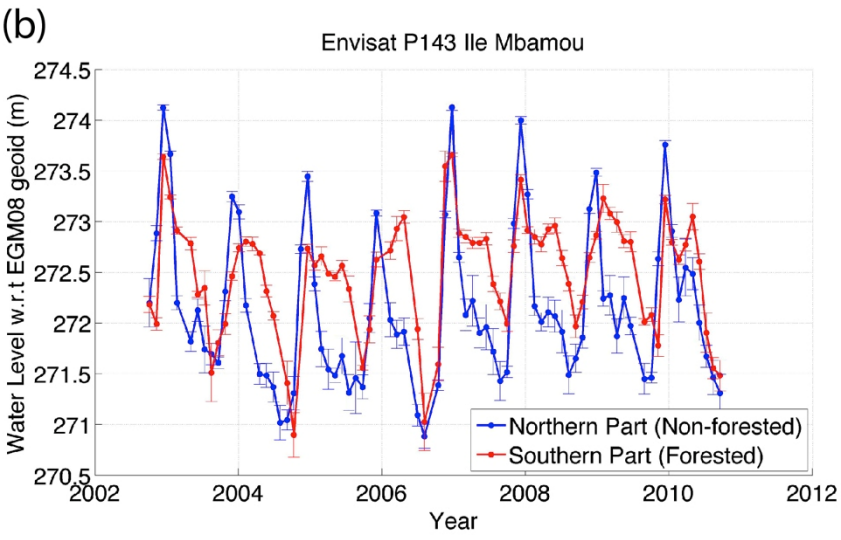

Figure 4. (**a**) Time series of water level changes from Envisat altimetry over the southern Congo River (region "1", blue) and from the daily *in situ* gauge at Brazzaville (red). The black dots indicate the daily *in situ* data temporally closest to the Envisat altimetry data, which are used to compute RMSE and correlation coefficient; (**b**) Time series of water level changes from Envisat altimetry over the southern (region "2") and northern (region "3") parts of the Île Mbamou. Error bars represent 95% confidence intervals.

4.2. Comparison of Water Level Changes from Envisat Altimetry over the Everglades and in Situ *Data*

In order to demonstrate Envisat altimeter's capability of measuring water level changes over these vegetated wetlands in the Île Mbamou where no *in situ* record exists, we first performed indirect verification by comparing the Envisat altimetry derived water level changes and *in situ* records over the Everglades wetlands in Florida, USA. We also performed a comparison between Envisat altimetry derived water level changes and InSAR-derived water level changes over the forested southern the Île Mbamou which will be shown in Section 5.3. Figure 5 shows Envisat ground tracks over the Everglades with its VCF as background. We generated six water level change time series using the 18-Hz ICE-1 retracked measurements from passes 194 and 465, and compared them with nearby gauge data. As summarized in Table 2, VCF values extracted over the Envisat stations indicate that stations EnvP194_1, EnvP194_2, EnvP194_3, EnvP194_4, and EnvP465 are covered with non-forested vegetation and station EnvP194_5 is covered with forested vegetation. Figure 6 and Table 2 show that all of the Envisat altimetry time series agree very well with *in situ* data regardless of the canopy density. The unstable performance of Envisat altimetry over EnvP194_3 in 2007 and 2009 is expected to be due to the dry conditions of the surface that persisted about three months as can be seen from *in situ* data. After all, although the forest types in the Everglades and the southern Île Mbamou may be different, this comparison study over the Everglades shows that Envisat altimetry can measure water level changes beneath both non-forested and forested land cover accurately.

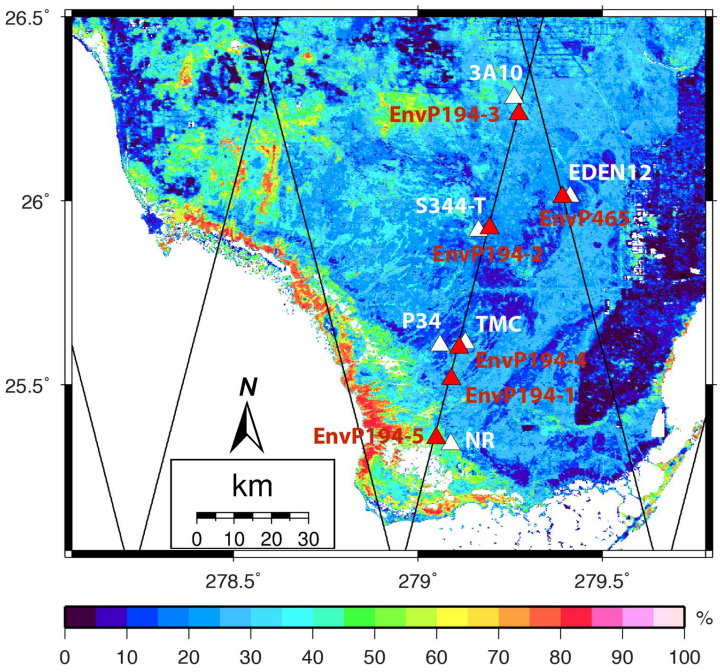

Figure 5. VCF Map of the Everglades with Envisat ground tracks. The Envisat stations and adjacent *in situ* gauges are indicated with red and white triangles, respectively.

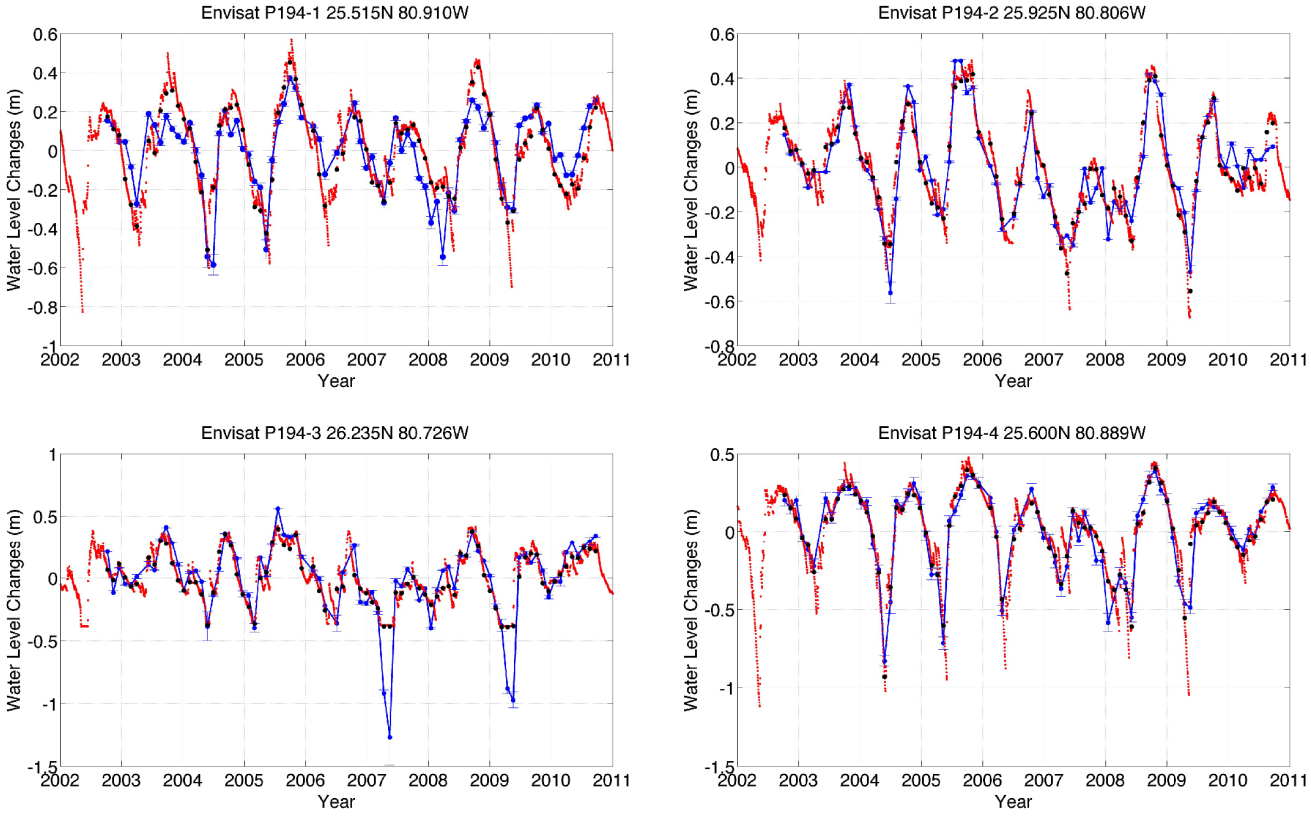

Figure 6. *Cont.*

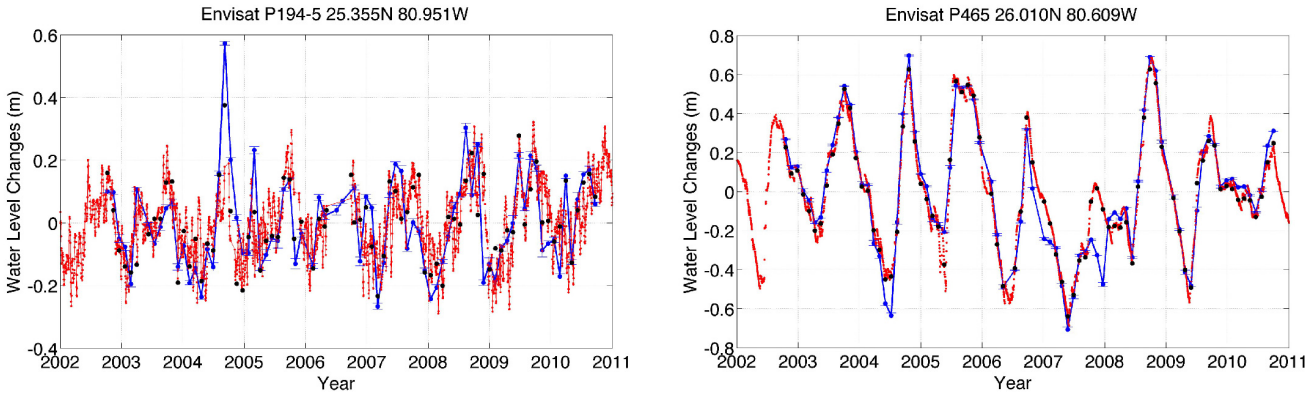

Figure 6. Time series of water level changes from Envisat altimetry (blue) and nearby *in situ* gauges (red). The black dots indicate the *in situ* data temporally closest to the Envisat altimetry data, which are used to compute RMSE and correlation coefficient.

Table 2. Comparison between water level changes obtained from Envisat altimetry and *in situ* data over the Everglades wetlands.

Altimetry Time Series	*In Situ* Gauges	Distances between the Altimetry Station and Gauge (km)	RMSE (cm)	Correlation Coefficient	VCF (%)
EnvP194-1	P34	10.7	12.2	0.83	25
EnvP194-2	S344-T	3.2	8.6	0.92	19
EnvP194-3	3A10	5.1	17.1	0.87	27
EnvP194-4	TMC	2.3	8.0	0.97	29
EnvP194-5	NR	4.4	9.8	0.75	48
EnvP465	EDEN12	2.1	8.6	0.96	21

4.3. Water Level Changes over Each Envisat's High-Rate Nominal Footprint

Next, we generated water level change time series over each of Envisat's 18-Hz nominal ground track location using the high-rate *stackfile* method (for details, refer to [22,40]). Each Envisat high-rate (18-Hz) *stackfile* bin serves as the 18-Hz nominal ground track to which the 18-Hz water level change time series are referred. For each GDR record from a given Envisat cycle and pass, the corresponding row is predicted based on an equator crossing table which is computed by interpolating the precision orbit ephemeris (POE) of Envisat. In other words, for example, for an ascending pass, the row can be computed such as [41]:

$$row_{asc} = \frac{T_{asc} - T_{eqAsc}}{\Delta T} \quad (2)$$

where, T_{asc} is the time tag on the ascending pass of a surface height measurement, T_{eqAsc} is the time tag when the ascending pass crosses the equator and ΔT is the time spacing of the surface height measurements. The equator crossing tables are the basis of mapping transformation between time tags in GDR record and row-column addresses of the low-rate (1-Hz) *stackfile* bins (for details, refer to Chapter 2 of [41]). If the predicted 1-Hz *stackfile* row-column address is equivalent to the given bin address of the empty *stackfile* array, then for each 1-Hz stackfile bin, 18-Hz *stackfile* bins (or 18-Hz nominal ground tracks), in which the water levels are "stacked", are created. The latitudes and longitudes

of the 18-Hz bins (or ground tracks) are calculated by linearly interpolating two adjacent 1-Hz nominal ground track latitudes and longitudes, which are stored in the 1-Hz *stackfile* bin header. The 18-Hz nominal ground tracks over the Île Mbamou are plotted in Figure 1a.

4.4. Water Level Changes from InSAR

To be compared with the water level changes from altimetry, we generated two differential interferograms using PALSAR pairs obtained on 26 October 2007–11 November 2007 (water increasing period) and 16 December 2009–31 January 2010 (water decreasing period), and obtained their spatial gradient of the water level changes between the acquisition dates (results in Section 5.3). Perpendicular and temporal baselines of the interferograms are summarized in Table 3. After flat-earth phase removal, the interferometric phase mainly contains contributions from the topographic relief and surface deformation in the radar range direction. The differential interferogram, which presumably contains phase changes only due to wetland water level changes [8,11,14] which correspond to the contribution from the deformation, were generated after removing the topographic phases using the SRTM DEM. Because inaccurate orbit vector information provided in the PALSAR metadata often leaves residual fringes in the interferograms, we modeled the baseline error using the best-fitting polynomial to remove the artifacts due to the orbital error. The differential interferograms were then smoothed using adaptive filtering to enhance the fringe visibility, and finally geocoded to yield the displacement maps using the look-up table generated from existing geocoded SRTM DEM and SAR image orbital information [42]. Considering the radar wavelength and incidence angle of the PALSAR images, 1.0 radian of interferometric phase is equivalent to 2.4 cm of vertical water level change [12].

Table 3. Description of InSAR pairs used to generate interferograms.

Attribute	Water Increasing Season	Water Decreasing Season
Perpendicular Baseline	116 m	79 m
Ambiguity height	439 m	645 m
Date	26 October 2007	16 December 2009
	11 December 2007	31 January 2010

5. Estimating Wetland Water Level Changes Based on σ_0 Changes

5.1. Temporal Variation of σ_0

Figure 7 shows the geocoded PALSAR σ_0 images over the study region. It is clear to see the temporal variations in the backscattered intensity, but with distinctly different patterns over the northern and southern parts of the Île Mbamou. For example, in June (10 June 2007 or 12 June 2008) which corresponds to the low-water season, the entire island reveals similar intensity while in December (11 December 2007, 13 December 2008, or 16 December 2009), the high-water season, the southern part appears much brighter than the northern part. This can be explained if the northern part of the island has mainly non-forested low canopy vegetation whereas the vegetation on the southern part is mainly highly dense forest as indicated by the VCF map in Figure 2. During the high-water season, the northern Île Mbamou (non-forested) would be mostly submerged and little radar energy would be backscattered to

the satellite due to specular scattering. On the other hand, over the southern Île Mbamou (forested), increasing water level would lead to stronger double-bounce backscattering.

As shown in Figure 8, the σ_0 over the northen and southern Île Mbamou (over the black boxes in the averaged σ_0 map in Figure 7) show seasonal variations which are expected to be related to the water level changes. Mostly, the peaks and troughs of the non-forested land σ_0 variation correspond to the troughs of peaks of the forested land σ_0 variation, respectively. In case of the forested land, increasing water level leads to stronger radar return due to enhanced double-bounce backscattering. On the contrary, the radar backscattering over the non-forested land is governed by the specular scattering during high-water season, leading to weaker radar return. However, stronger radar return is observed during the low-water season due to the double-bounce backscattering [11,21] or multipath backscattering [17] in non-forested vegetation. From Figure 8, it is also noted that σ_0 over the non-forested northern Île Mbamou reveal stronger temporal variation than those over the forested southern Île Mbamou.

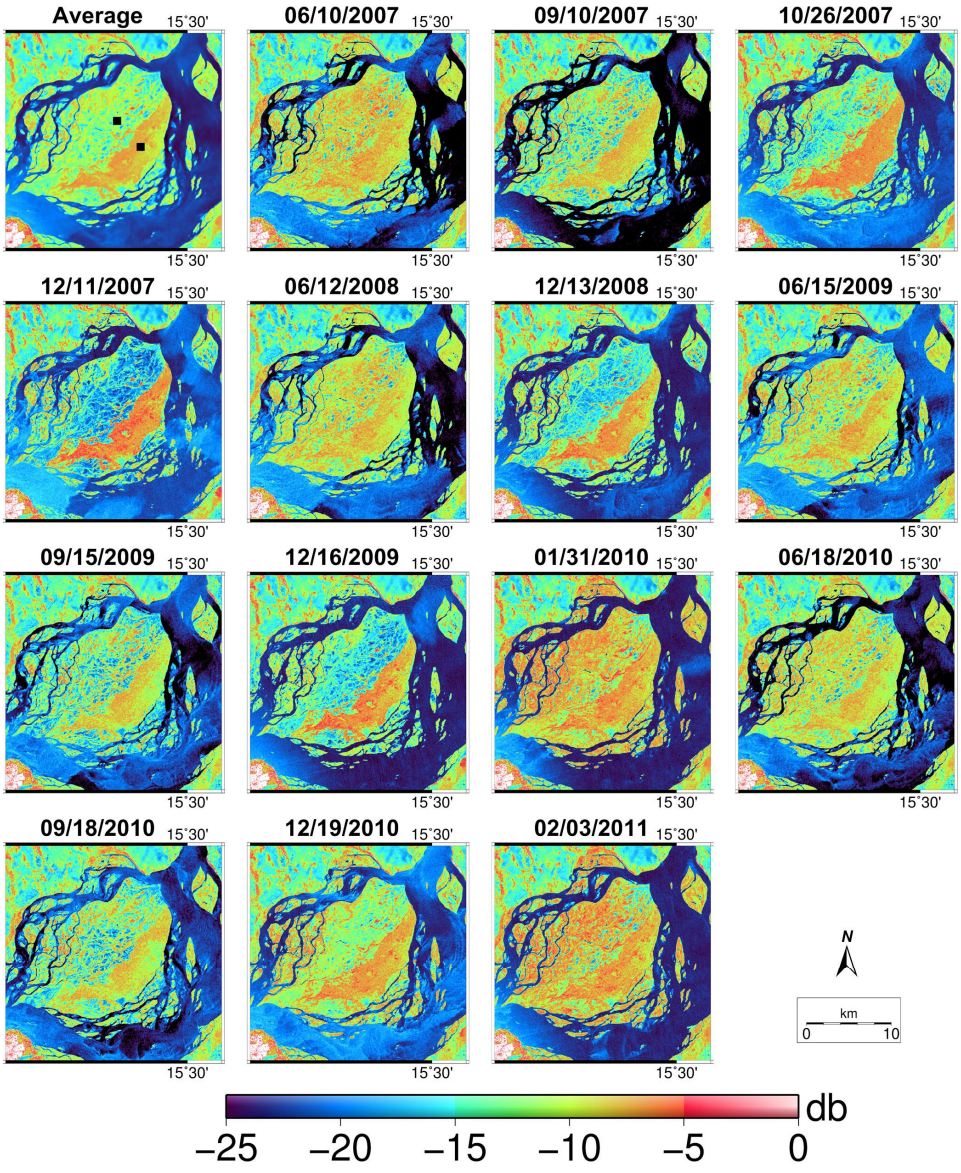

Figure 7. Images of PALSAR σ_0 used in this study. PALSAR σ_0 values over the northern part of the island, and the southern part of the island marked with black boxes in the "Average" image are used for Figure 8.

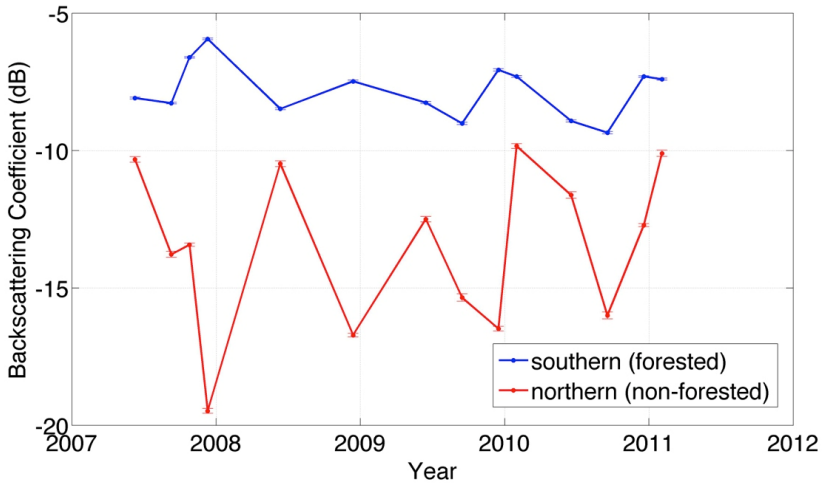

Figure 8. Variations of PALSAR σ_0 over the northern and southern parts of the island, averaged over the 31 × 31 black boxes shown in Figure 7. Error bars represent 95% confidence intervals.

It is noted that another important driver of temporal variation in L-band σ_0 over non-forested vegetation is variation in soil moisture [17]. It is expected that σ_0 would increase if the surface soil condition transits from dry to wet. Although the northern Île Mbamou may experience seasonal dry condition, we expect that the σ_0 variation observed in Figures 7 and 8 is not likely due to the soil moisture variation based on Figure 9 which compares the time series of Envisat water level changes and PASLAR σ_0 changes over the northern Île Mbamou. As can be seen, PALSAR σ_0 increases when the water level decreases. In other words, when we observe the increase in PALSAR σ_0 occurs not during the dry or early wet period, but during the decreasing water period due to the enhanced double-bounce (or multipath) backscattering. Therefore, the PALSAR σ_0 data that we used in this study (listed in Table 1) do not show variation due to the soil moisture increase, at least over the Envisat altimetry footprint locations.

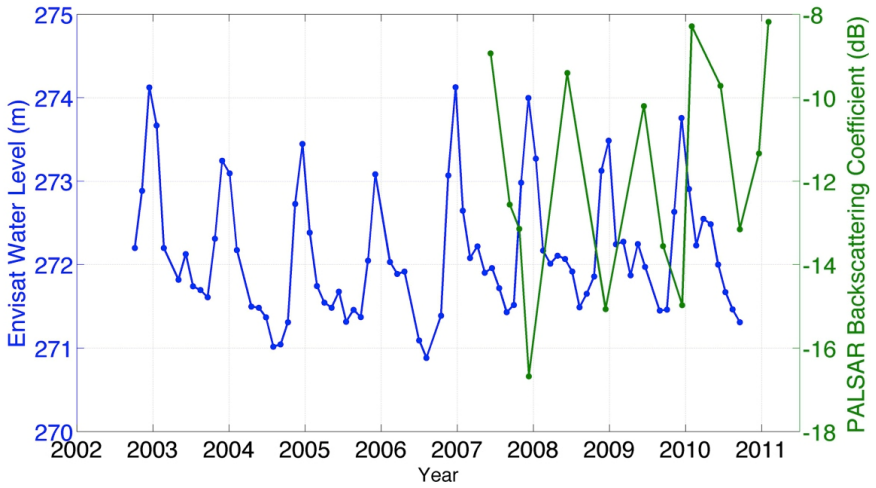

Figure 9. Time series of water levels from Envisat altimetry (blue, left-axis) and backscattering coefficient from PALSAR (green, right-axis) over the non-forested northern Île Mbamou.

5.2. Effects of Water Level Changes on PALSAR σ_0

5.2.1. Relationship between Envisat Water Level Changes and PALSAR σ_0 Changes

Here, we performed linear regression analysis between water level changes from Envisat altimetry and PALSAR σ_0 changes over each Envisat's 18-Hz nominal ground track (or footprint) location. The σ_0 changes over the ground track locations were obtained by performing a bilinear spatial interpolation. The water level changes generated over each of the 18-Hz *stackfile* bins are linearly interpolated to each PALSAR acquisition dates using two consecutive water level changes obtained before and after the acquisition dates, and compared with the corresponding PALSAR σ_0 changes. For each Envisat's 18-Hz nominal footprint, we used the lowest water level as a reference and performed regression analysis between the changes of water levels and σ_0 as shown in Figures 10 and 11. From Figure 10, we observe positive correlation between the changes of water levels and σ_0, which indicates that increasing water levels lead to stronger σ_0 over the forested lands. The stronger σ_0 can be explained by the enhanced double-bounce backscattering due to the increasing water levels. On the other hand, from Figure 11, we also observe the positive correlation between the changes of water levels and σ_0 over the non-forested lands until the water surface reaches a certain level. This can also be explained by the stronger double-bounce backscattering. If the water level continues to increase, then the negative correlation between the changes of water levels and σ_0 is observed over the non-forested lands, which can be explained by the enhanced specular backscattering. A schematic plot illustrating these different backscattering mechanisms is shown in Figure 12. The VCF threshold used to distinguish between the forested and non-forested lands will be discussed in the following section.

5.2.2. Distinguishing Forested and Non-Forested Lands

In Figures 10 and 11, we used the mean VCF as a representative vegetation density value at each of Envisat's 18-Hz nominal footprint location, so we can investigate the relation between the linear regression slopes and VCF as well (see Section 5.2.3). It is noted that the spatial resolution of VCF (250 m) is finer than the altimeter along-track footprint interval (~350 m). First of all, we need to determine a threshold to classify the forested and non-forested lands using VCF which is the percentage tree cover for every pixel. Various studies have used different VCF tree cover thresholds to determine forest land areas. For example, Nelson *et al.* [43] used a threshold of 25% and produced estimates of forested land area similar to inventory estimates for the entire United States (US) and for the conterminous US. Schmitt *et al.* [44] used 10% tree cover threshold and estimated global forest cover to be 39 million km^2. Over the entire Congo Basin, Hansen *et al.* [45] used VCF Landsat training data and four years of MODIS inputs to classify "non-treed" cover with a threshold of <10%. In this study, we attempted to decide the threshold to distinguish between the forested and non-forested lands based on the regression relationships between σ_0 and water level changes over each of the Envisat 18-Hz nominal footprints.

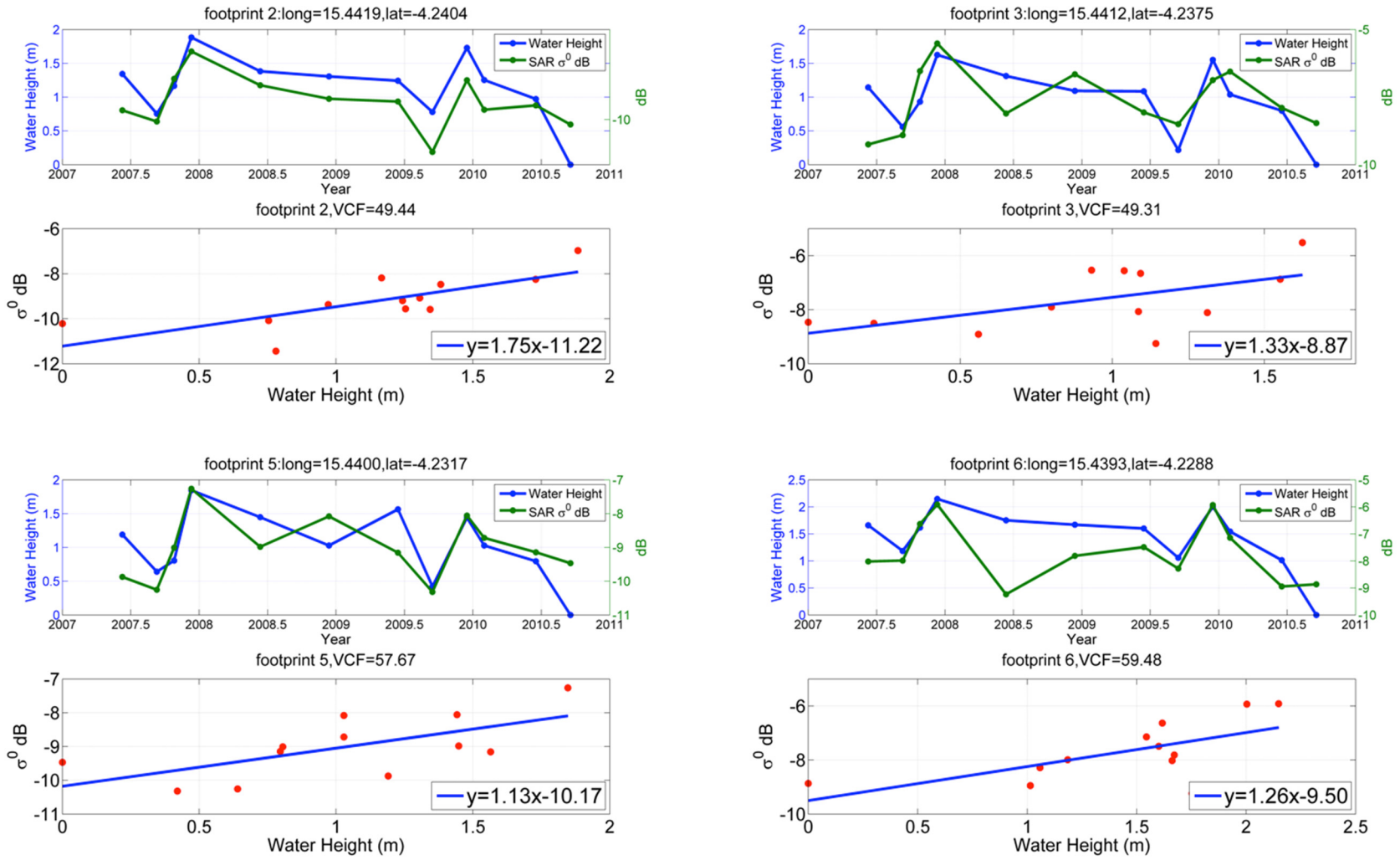

Figure 10. *Cont.*

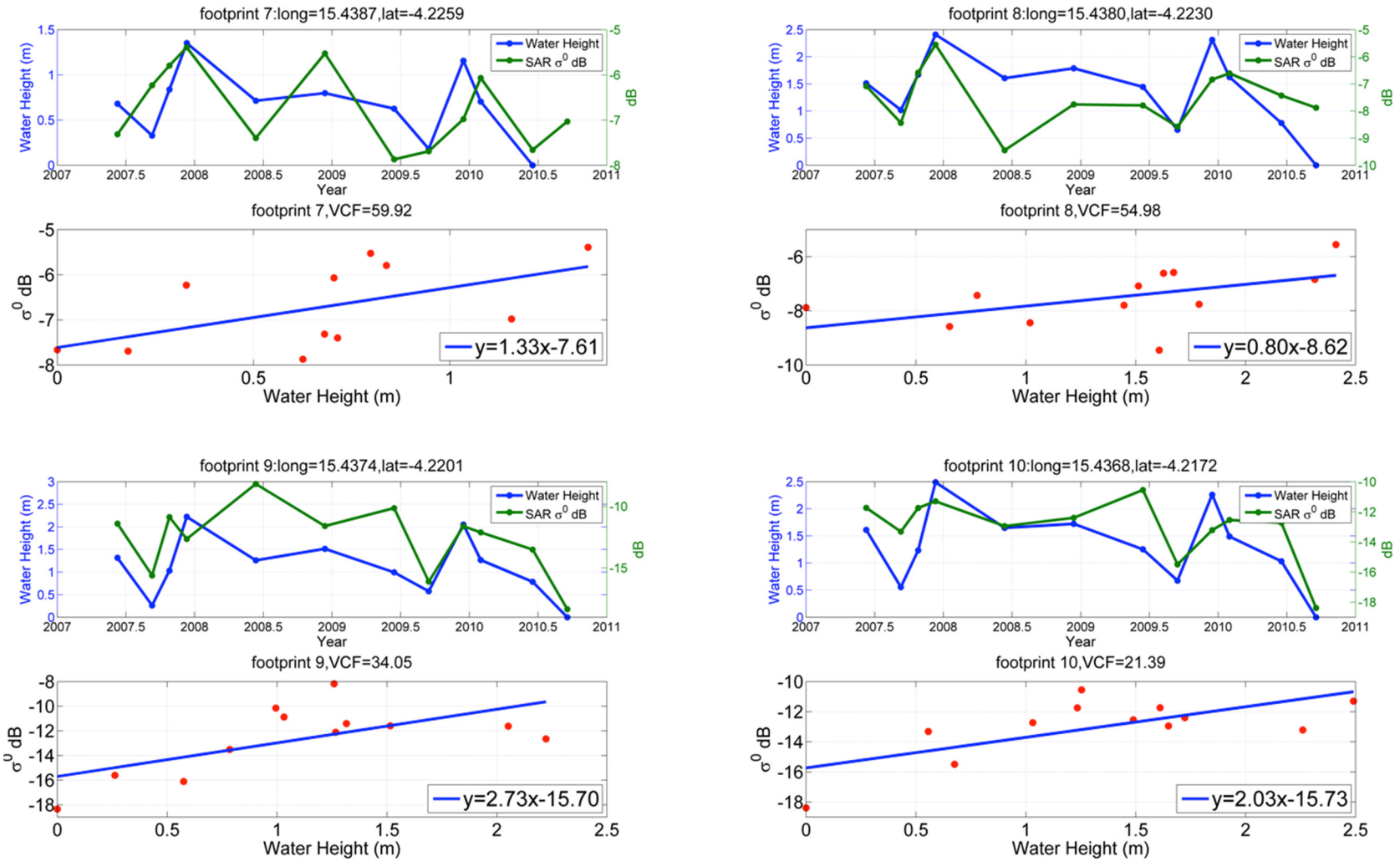

Figure 10. Selected time series of water level changes from Envisat altimetry (blue in the upper panels) and σ_0 (green in the upper panels) over the forested land. Results of linear regressions between them are illustrated in the bottom panels. The amplitude difference of the water level changes between adjacent 18-Hz nominal footprint is partially due to the altimeter measurement error. Refer to Figure 2 for the location of the footprints.

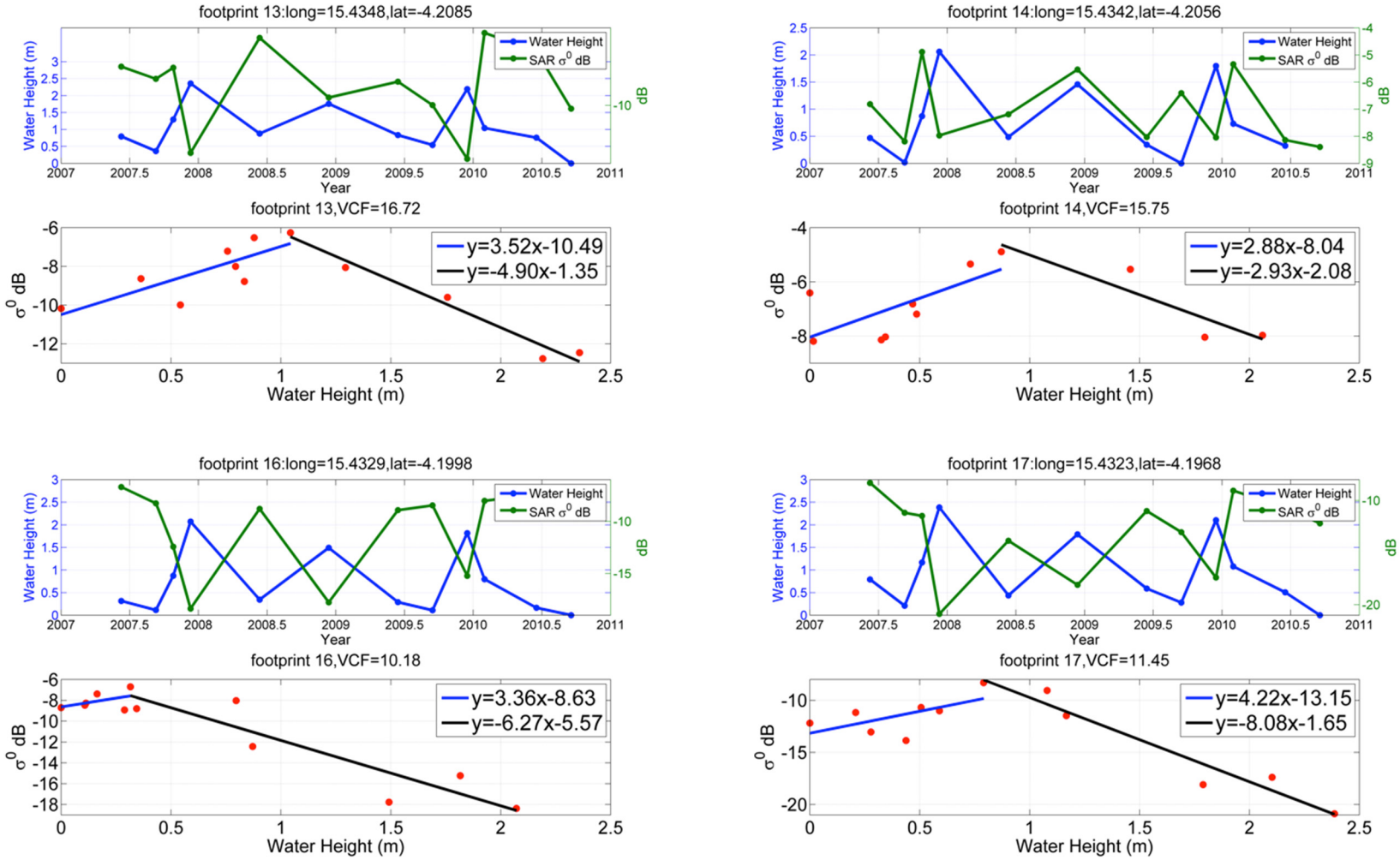

Figure 11. *Cont.*

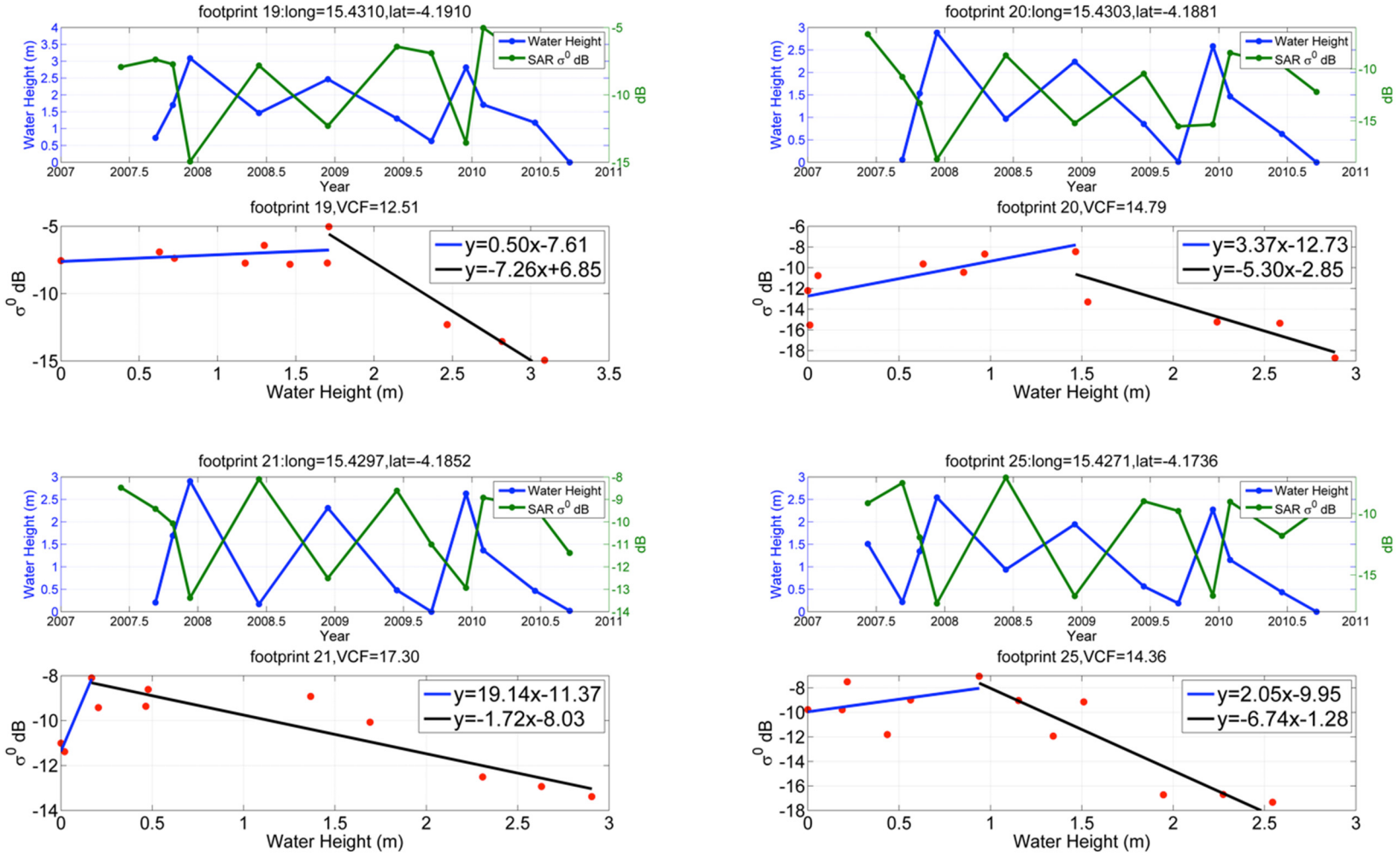

Figure 11. Selected time series of water level changes from Envisat altimetry (blue in the upper panels) and σ_0 (green in the upper panels) over the non-forested land. Results of linear regressions between them are illustrated in the bottom panels. The blue and black lines represent the fitted line for "water increase I", and "water increase II", respectively. The amplitude difference of the water level changes between adjacent 18-Hz nominal footprint is partially due to the altimeter measurement error. Refer to Figure 2 for the location of the footprints.

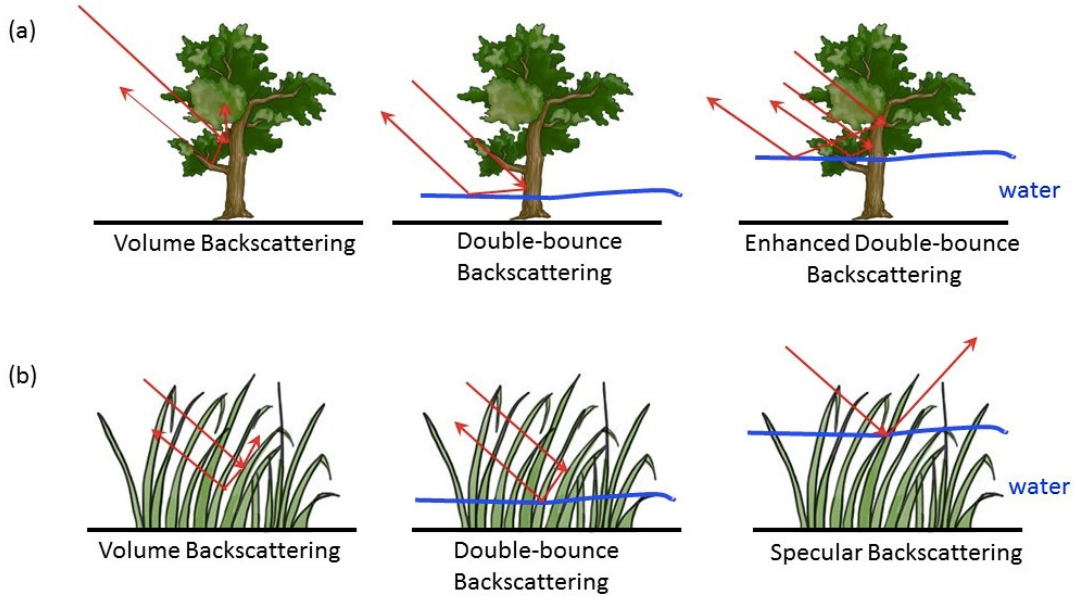

Figure 12. Different backscattering mechanisms over the (**a**) forested and (**b**) non-forested lands with different levels of water (modified from Figure 3 of [21]).

Figure 10 shows the time series of PALSAR σ_0 and interpolated Envisat altimetry water level changes over, for example, some of the footprint locations (footprints 2, 3, 5, 6, 7, 8, 9 and 10) which have VCF > 20%. We observe that there exists positive correlation between σ_0 and Envisat altimetry water level changes over these locations. In other words, higher water level leads to higher σ_0. This indicates that higher water level can lead to enhanced double-bounce backscattering over wetlands with VCF > 20%. The results of linear regressions are summarized in Table 4. Except for footprint 4, all of the locations with VCF > 20% have positive regression slopes. On the other hand, Figure 11, for example, shows the time series of σ_0 and interpolated Envisat altimetry water level changes over some of the footprint locations (footprints 13,14, 16, 17, 19, 20, 21 and 25) which have VCF < 20%. Interestingly, we found that both positive and negative correlations exist between σ_0 and water level changes. As water level increases up to ~1 m, σ_0 also increases as in the case of wetlands with VCF > 20%. However, when the water level increases more than ~1 m, σ_0 then starts to decrease. This can be explained if the double-bounce backscattering is enhanced with increasing water level only until a certain stage, and then specular backscattering becomes dominant with higher water levels over non-forested land. This finding is different from previous studies of [17,21] which employed only one regression model with a negative slope. Accordingly, we fitted two linear regression models: one with a positive slope and the other with a negative slope as shown in the bottom panels of Figure 11. The water level change which leads to the highest σ_0 is used to split the water level change and σ_0 variables, so the two regression models can be applied separately. Our regression results for all of the footprint locations with VCF < 20% are summarized in Table 5. Based on these observed different sensitivities of σ_0, the VCF threshold of 20% will be used in the following sections to distinguish the forested and non-forested land covers.

Table 4. Linear regression results over the southern forested Île Mbamou. Locations of Envisat 18-Hz nominal footprints are illustrated in Figure 2.

Envisat Footprint	Latitude (Degree)	Longitude (Degree)	VCF (%)	Slope	Intercept	R^2
1	15.4425	−4.2434	48.9	1.33	−9.29	0.15
2	15.4419	−4.2404	49.4	1.75	−11.2	0.56
3	15.4412	−4.2375	49.3	1.33	−8.86	0.32
4	15.4406	−4.2346	51.2	−0.23	−7.83	0.01
5	15.44	−4.2317	57.6	1.12	−10.17	0.41
6	15.4393	−4.2288	59.4	1.25	−9.49	0.41
7	15.4387	−4.2259	59.9	1.32	−7.6	0.31
8	15.438	−4.223	54.9	0.8	−8.62	0.27
9	15.4374	−4.2201	34.0	2.72	−15.69	0.4
10	15.4368	−4.2172	21.3	2.03	−15.73	0.46

Table 5. Linear regression results over the northern non-forested Île Mbamou. Locations of Envisat 18-Hz nominal footprints are illustrated in Figure 2.

Envisat Footprint	Latitude (Degree)	Longitude (Degree)	VCF (%)	Slope 1	Intercept 1	R^2	Slope 2	Intercept 2	R^2
11	15.4361	−4.2143	19.0	2.97	−16.71	0.74	−10.48	6.25	0.95
12	15.4355	−4.2114	15.4	8.58	−23.68	0.66	−9.83	2.36	0.82
13	15.4348	−4.2085	16.7	3.51	−10.49	0.64	−4.90	−1.35	0.96
14	15.4342	−4.2056	15.7	2.87	−8.041	0.48	−2.93	−2.07	0.84
15	15.4335	−4.2027	13.7	0.50	−8.48	0.02	−7.84	0.73	0.95
16	15.4329	−4.1998	10.1	3.35	−8.67	0.22	−6.27	−5.56	0.84
17	15.4323	−4.1968	11.4	4.21	−13.15	0.37	−8.08	−1.64	0.94
18	15.4316	−4.1939	12.6	1.25	−8.95	0.44	−3.95	−6.69	0.66
19	15.431	−4.191	12.5	0.49	−7.60	0.10	−7.26	6.84	0.96
20	15.4303	−4.1881	14.7	3.36	−12.73	0.61	−5.29	−2.85	0.78
21	15.4297	−4.1852	17.2	19.14	−11.36	0.95	−1.72	−8.02	0.85
22	15.4291	−4.1823	15.6	2.33	−12.20	0.23	−6.34	−0.04	0.73
23	15.4284	−4.1794	17.4	2.79	−10.91	0.81	−3.41	−4.20	0.50
24	15.4278	−4.1765	15.8	−2.13	−7.28	0.22	−17.06	29.91	0.99
25	15.4271	−4.1736	14.3	2.04	−9.94	0.16	−6.74	−1.27	0.86
26	15.4265	−4.1707	16.1	1.98	−9.70	0.34	−5.22	−4.63	0.60

5.2.3. Relationship between the σ_0 Sensitivity and VCF

Different regression slopes (dB/m) summarized in Tables 4 and 5 over each of the footprints indicate varying sensitivities of σ_0 to water level changes over the forested and non-forested lands. For example, a steeper regression slope indicates higher σ_0 sensitivity to water level changes. Here, we examined the relation of the σ_0 sensitivity and VCF over the forested and non-forested lands, separately. Figure 13 shows the relation between the regression slopes and VCF values over each of the footprints in forest (VCF > 20%). We observe that the regression slope (or σ_0 sensitivity) generally decreases with higher VCF (between 20% and 60%). This can be explained if denser canopy leads to higher volume scattering from the canopy and less double-bounce backscattering with less radar energy that penetrate through

denser canopy. In other words, although the same amount of water level increase occurs, a smaller amount of σ_0 increase is obtained if the area is covered with denser canopy.

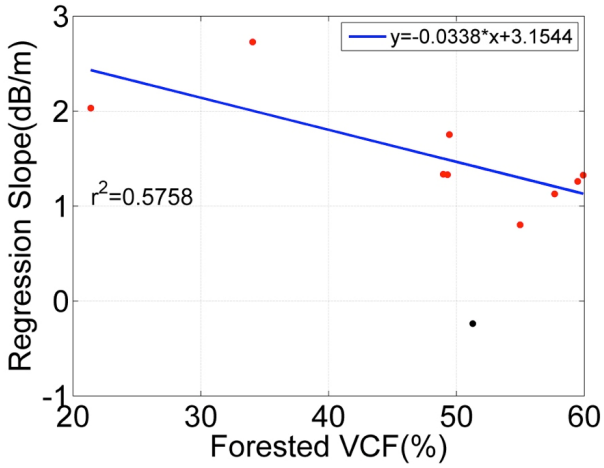

Figure 13. Regression analysis between the regression slope (dB/m) from Table 4 and VCF over the forested land. Black dot is treated as an outlier and excluded from the regression analysis.

On the other hand, in the non-forested land, as mentioned above, σ_0 first increases, then decreases as the water level increases. Here, we have separated the σ_0 response to water level changes with respect to the water level increase which yields the highest σ_0. Saturation point of σ_0, which is described in [46,47] is generally determined by above-water biomass and above-water canopy height. Figure 14 shows the relationship between the water increase yielding the highest σ_0 (or "saturation height") and the corresponding VCF value in the non-forested land (between 10% and 20%). Generally, we see that higher VCF results in higher saturation height. In fact, this positive correlation is consistent with the conclusion drawn from [46,47] which used above-water biomass and above-water canopy height. The positive correlation indicates that higher VCF area would need higher water level to reach the saturation biomass and hence higher saturation height. Next, to examine the σ_0 sensitivity in the non-forested land, we first divided the total span of water level increases into two parts: "water increase I" ($0 < h <$ saturation height) and "water increase II" (saturation height $< h < h_{max}$), and performed linear regression between the σ_0 sensitivity and VCF as done in forest (Figure 13). Figure 15a shows the relationship between the σ_0 sensitivity to "water increase I" and non-forest VCF, and no obvious relationship can be observed. This indicates that the density of the non-forested vegetation do not have influence on the σ_0 sensitivity (or the double-bounce backscattering for "water increase I"). For "water increase II", as shown in Figure 15b, a positive correlation between σ_0 sensitivity and VCF can be found, indicating that lower non-forested vegetation density leads to steeper regression (negative) slope. In other words, the specular scattering which leads to little radar return to the satellite is enhanced with less dense non-forested canopy. It should be noted that the regression slopes are all negative for "water increase II" when water level increase exceeds the saturation height because the specular scattering becomes dominant as the canopy becomes submerged, and there is little chance for radar signal to interact between canopy stems and water surface [48].

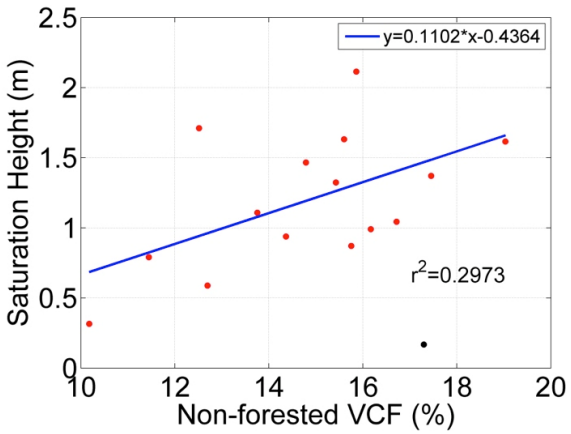

Figure 14. Relation between saturation height and VCF in the non-forested land. The black dot is treated as an outlier and excluded from the regression analysis.

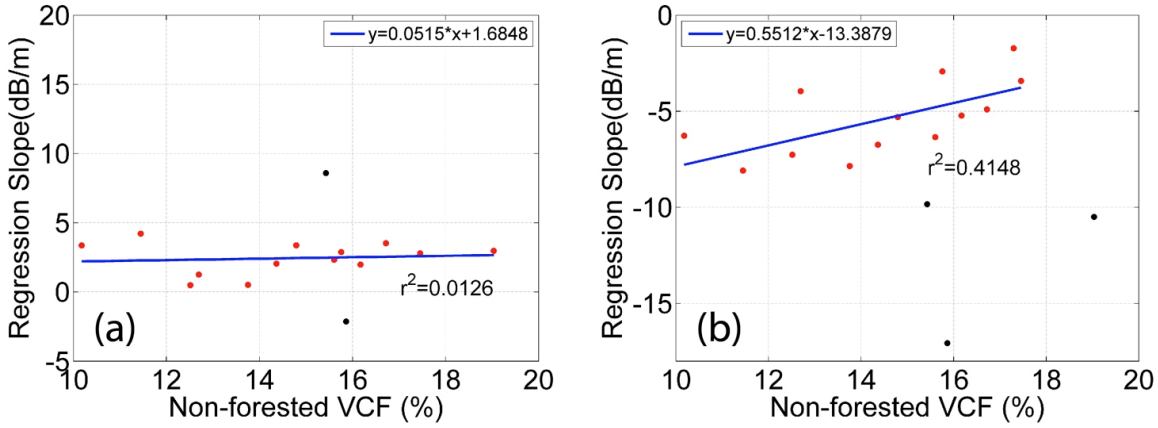

Figure 15. (**a**) Regression analysis between the regression slope1 (dB/m) from Table 5 and VCF over the non-forested land for "water increase I"; (**b**) Regression analysis between the regression slope2 (dB/m) from Table 5 and VCF over the non-forested land for "water increase II". Black dots are treated as outliers and excluded from the regression analysis.

It is noted that the outliers excluded from the regression analyses in Figures 13–15 are caused by the altimeter measurement errors or by the coarse spatial resolution of the VCF product.

5.3. Water Level Changes Estimated from σ_0 Changes and VCF

In this section, based on the σ_0 sensitivities characterized over the Île Mbamou, we attempted to estimate water level changes between two pairs of SAR acquisition dates: one for the water increasing period (26 October 2007–11 December 2007) and the other for the water decreasing period (16 December 2009–31 January 2010), which are the same SAR pairs used to generate the two differential interferograms described in Section 4.4. We first arbitrarily selected 14 Envisat footprint locations among the 26 footprint locations: five over the forested, and nine over the non-forested lands (green circles in Figure 18) for the purpose of performing the regression analysis as shown in Figure 16 on the σ_0 sensitivity (or the regression slope of dB/m) and VCF over forested and non-forested lands, separately, similar to the analysis done in Figures 13 and 15, respectively. The rest of the footprints will be used to perform comparison with the Envisat altimetry water level changes for validation purpose.

Next, using the regression result (dB/m *versus* VCF) from Figure 16, we computed the water level changes over the 18-Hz Envisat footprints which were *not* used for the regression analysis (purple diamonds in Figure 18) such as:

$$\Delta h = \frac{\Delta\sigma_0}{(Regression\ Slope) \cdot VCF}\ (m) \tag{3}$$

where $\Delta\sigma_0$ (dB) is the σ_0 changes between the two dates, and the regression slope has a unit of dB/m/VCF(%) determined from Figure 16.

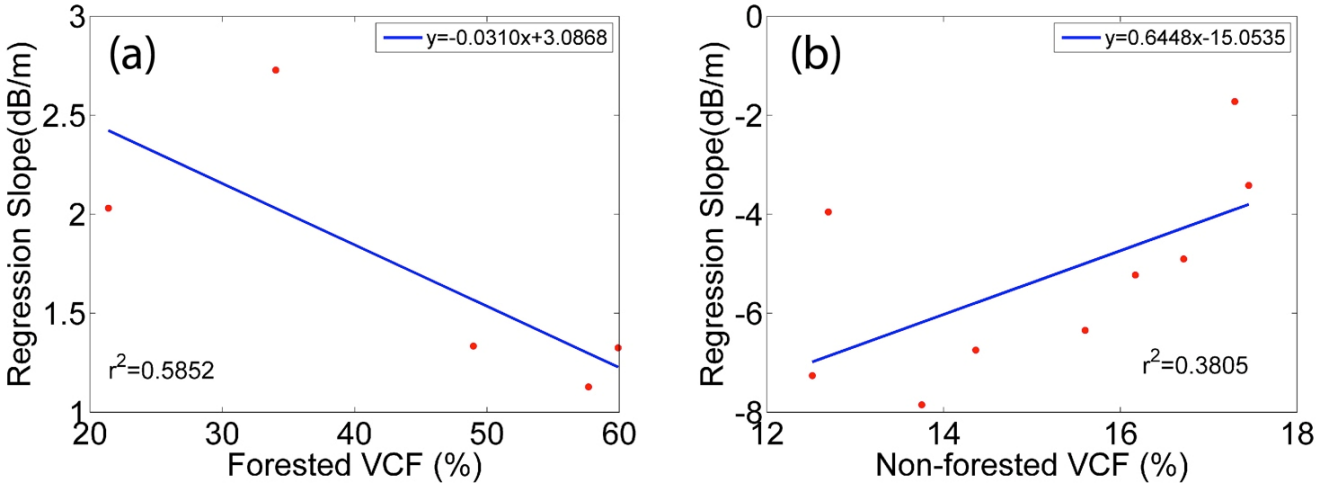

Figure 16. Regression analysis between the regression slopes (dB/m) and VCF using five Envisat footprints over the forested land and nine Envisat footprints over the non-forested land.

Before we compare the estimated Δh from Equation (3) with Δh obtained from Envisat altimetry water levels, we first compared Δh from InSAR which has a centrimetric accuracy [49] and Δh from Envisat altimetry in order to further validate the altimetry results. Figure 17 shows the two wrapped differential interferograms generated over the forested area. Due to low coherences, the fringes over the non-forested area have been masked out, and we were able to validate altimetry measurements over the forested southern Île Mbamou only. The interferogram shown in Figure 17a reveals a spatial variation in water level change between 26 October 2007 and 11 December 2007 whereas the interferogram in Figure 17b shows negligible spatial variation in water level change between 16 December 2009 and 31 January 2010. The differential interferometric phases along the Envisat 18-Hz footprints (black lines in Figure 17) have been extracted, unwrapped, and converted to vertical displacements. Since InSAR can measure only spatially relative water level changes, arbitrary constants (+0.766 m and −0.441 m for Figure 17a,b, respectively) have been added (red "+" in Figure 18) for better comparison with Envisat altimetry results in Figure 18. The InSAR and Envisat altimetry water level changes agreed quite well with Root-Mean-Square-Error (RMSE) of 18.3 cm and 9.7 cm for the interferograms in Figure 17a,b, respectively. This further validates altimetry's capability of measuring water level changes beneath dense forest canopy.

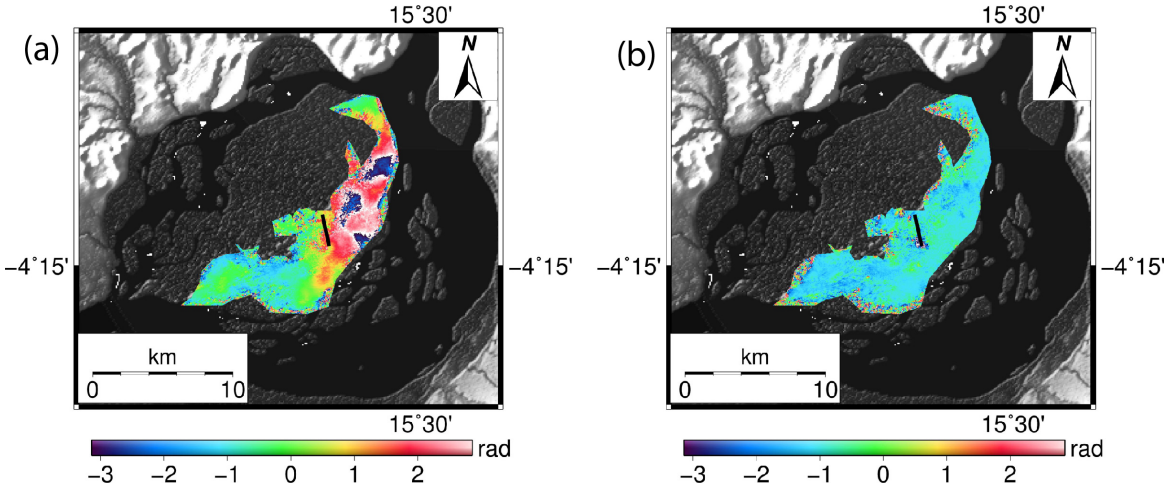

Figure 17. Wrapped differential interferograms over the Île Mbamou representing water level changes over the southern forested land between (**a**) 26 October 2007–11 December 2007; and (**b**) 16 December 2009–31 January 2010.

Next, we compared Δh obtained from Equation (2) and Envisat altimetry over the footprint locations indicated with purple diamonds in Figure 18. Their differences are listed in Table 6. We obtained mean RMSEs of 48.95 cm for the period of 26 October 2007–11 December 2007 and 64.69 cm for the period of 16 December 2009–31 January 2010 over the forested area. The large difference between Δh from Equation (2) and altimetry shown in red box in Figure 18, which indicates the boundary between the forested and non-forested areas, could be caused by the error of VCF product in distinguishing different vegetation densities with its coarser spatial resolution (~250 m) than PALSAR (~30 m). If we exclude those footprints (footprints 11 and 12), we obtain RMSEs of 37.86 cm for the period of 26 October 2007–11 December 2007, and 58.80 cm for the period of 16 December 2009–31 January 2010 in the non-forested area which is comparable with the result in [19] that achieved 22 cm RMSE for the estimated water levels over marshes in the Parana Basin using Envisat ASAR σ_0 and electromagnetic models that address the vegetation structure and interaction mechanism. It is noted that our approach does not rely on any electromagnetic models requiring detailed vegetation properties [18,19] or *in situ* measurements [21]that may be rarely available over the remote river basins.

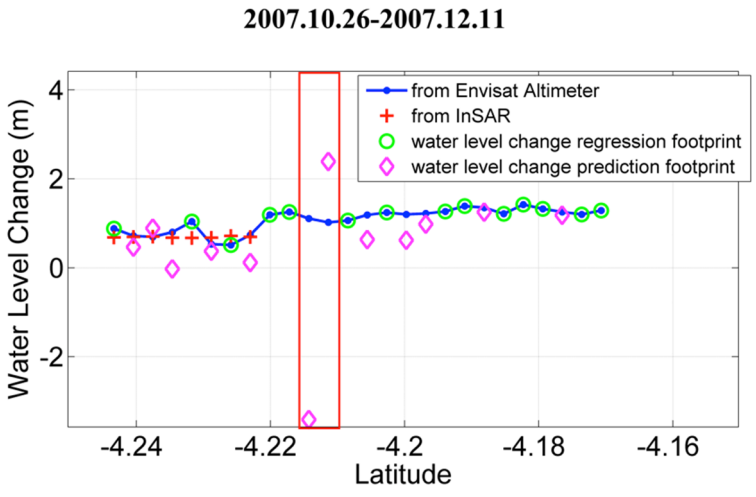

Figure 18. *Cont.*

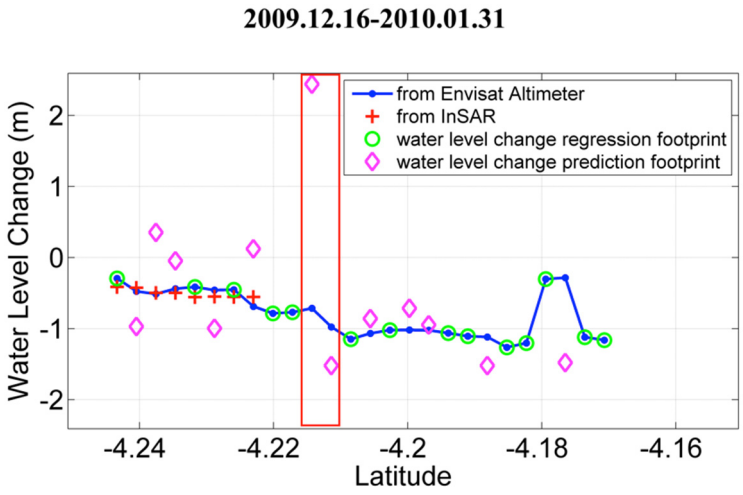

Figure 18. Comparison of water level changes obtained from Envisat altimetry (blue dots), InSAR (red pluses) and model predicted using Equation (2) (magenta diamonds). Green dots represent the footprint locations where Envisat altimetry water level changes and σ_0 are used to construct the regression model in Figure 16.

Table 6. Differences of Δh obtained from Equation (2) and Envisat altimetry over the footprint locations indicated with purple diamonds in Figure 18. Values in parentheses indicate the differences over the footprints located in the boundary of the forested and non-forested lands that were excluded in the RMSE computation.

	Differences for the Period of 26 October 2007–11 December 2007 (cm)	**Differences for the Period of 16 December 2009–31 January 2010 (cm)**
Forested Land	25.35	49.44
	−19.75	−86.56
	82.80	−39.20
	15.94	53.77
	61.97	−80.99
RMSE	48.95	64.69
Non-Forested Land	(452.42)	(−315.31)
	(−136.88)	(54.33)
	55.48	−20.67
	57.98	−30.43
	23.87	−7.70
	10.06	40.32
	7.56	119.36
RMSE	37.86	58.80

6. Application Discussion

In order to demonstrate that our method can be applied to other wetlands, we performed a similar sensitivity analysis over the Everglades wetlands. We utilized the regression slopes obtained using *in situ* water level changes and PALSAR σ_0 changes over six gauge locations (six red dots in Figure 19) in the non-forested, sawgrass-dominated Water Conservation Areas (WCAs) from Figure 4 of [21]

(using Path 149 results). We extracted the VCF values over those six gauge locations and performed a similar sensitivity analysis as we did in Figure 15. As can be seen from Figure 19, we obtained a similar positive correlation between the VCF and the regression slopes (dB/m) as we did in Figure 15b. Therefore, although it was not possible to perform similar analysis over other forested areas due to the lack of *in situ* data, it is expected that we can estimate water level changes over wetlands based on different L-band σ_0 responses to water level changes in different vegetation fields.

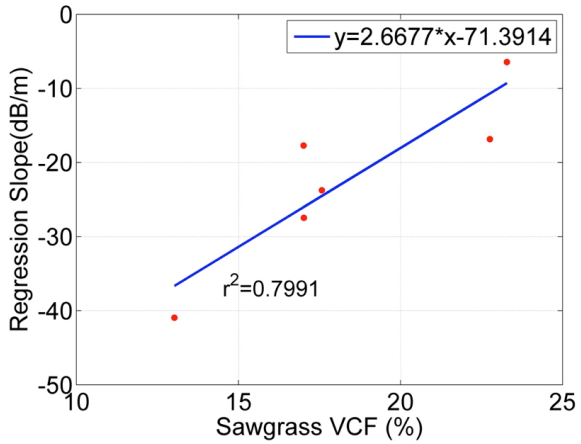

Figure 19. Regression analysis between the regression slopes (dB/m) and VCF over the six gauges located over the sawgrass-dominated Everglades wetlands. The regression slopes were obtained from Figure 4 of [21].

7. Conclusions

This paper describes the seasonal variations of PALSAR σ_0 over the wetlands in the island of Île Mbamou where two distinctly different vegetation types are found, and its relations with water level changes obtained from Envisat altimetry have been investigated. We obtained positive correlation between σ_0 and water level changes over the forested land whereas both positive and negative correlations are observed over the non-forested land depending on the amount of water level increase. It was shown that the PALSAR backscatter response is enhanced during early water increasing season and then diminished with more increase in water level over the non-forested land. We also performed the analysis of σ_0 sensitivity, and found that denser vegetation canopy leads to less sensitive σ_0 variation with respect to the water level changes regardless of the vegetation type (forested or non-forested). Furthermore, based on the σ_0 sensitivity analysis, we also attempted to estimate water level changes which were then compared with the Envisat altimetry measurements, and obtained respective mean RMSEs of 57 cm and 48 cm over the forested and the non-forested lands, obtained by excluding the boundary footprints. Possible error sources include Envisat altimetry interpolation error, speckle noise in σ_0, resolution mismatch between σ_0 and VCF, and uncertainties in linear regressions. However, if we consider most of the contemporary floodplain hydrodynamic modeling has a scale of several hundred meters [50,51] our overall mean RMSE of 53 cm at 30-m scale (SAR resolution), which can be interpreted as 5.3 cm RMSE at 300-m scale if the pixel-to-pixel noise is uncorrelated, shows that our method can be useful for calibration and validation of a hydrodynamic model.

For a future study, two-dimensional map of water level changes obtained from Equation (2) can be generated. To do so, it is noted that a more detailed VCF-like map, which has a high spatial resolution similar to that of SAR image, is needed to estimate the water level change at each of SAR pixel. Although the map will not have the centrimetric accuracy as the repeat-pass InSAR provides, it would be still useful over wetlands with low canopy such as the non-forested areas, where InSAR loses its coherence and thus interferograms cannot be generated. On the other hand, our method can also provide a useful independent dataset for the planned Surface Water Ocean Topography (SWOT) satellite mission which is a single-pass Ka-band radar interferometer that will provide simultaneous measurements of water levels and inundated area for inland water bodies. Currently, InSAR is the only tool that can provide comparable dataset for SWOT observations over the wetlands. However, again, as can be seen in Figure 17, interferometric coherence cannot be maintained over the non-forested land, and InSAR requires a stable corner-reflector such as tree trunks to maintain interferometric coherence over the wetlands [11].

Acknowledgments

This research was supported by NASA's GRACE Program (NNX12AJ95G), Terrestrial Hydrology Program (NNX12AQ36G), and New Investigator Program (NNX14AI01G). ALOS PALSAR images are copyrighted JAXA and provided by Alaska Satellite Facility (ASF). Envisat altimetry data were provided by European Space Agency (ESA). *In situ* gauge data at Brazzaville was provided by Frederique Seyler. *In situ* gauge data over the Everglades was obtained from the Everglades Depth Estimation Network (http://sofia.usgs.gov/eden/stationlist-area.php?area=ENP). We also thank three anonymous reviewers for their constructive comments.

Author Contributions

Ting Yuan performed the main data analysis, and wrote most of the manuscript. Hyongki Lee processed the Envisat altimetry data. Hahn Chul Jung contributed to the InSAR data processing description.

Conflicts of Interest

The authors declare no conflict of interest.

References

1. Barbier, E.B. Valuing environmental functions: Tropical wetlands. *Land Econ.* **1994**, *70*, 155–173.
2. Hayashi, M.; van der Kamp, G.; Rudolph, D.L. Water and solute transfer between a prairie wetland and adjacent uplands, 2. Chloride cycle. *J Hydrol.* **1998**, *207*, 56–67.
3. Neue, H.U.; Gaunt, J.L.; Wang, Z.P.; Becker-Heidmann, P.; Quijano, C. Carbon in tropical wetlands. *Geoderma* **1997**, *79*, 163–185.
4. Mitsch, W.J.; Gosselink, J.G. *Wetlands*, 4th ed.; John Wiley and Sons: New York, NY, USA, 2007.

5. Jung, H.C.; Hamski, J.; Durand, M.; Alsdorf, D.; Hossain, F.; Lee, H.; Azad Hossain, A.K.M.; Hasan, K.; Khan, A.S.; Zeaul Hoque, A.K.M. Characterization of complex fluvial systems using remote sensing of spatial and temporal water level variations in the Amazon, Congo, and Brahmaputra rivers. *Earth Surf. Process. Landf.* **2010**, *35*, 294–304.
6. Beighley, R.E.; Ray, R.L.; He, Y.; Lee, H.; Schaller, L.; Andreadis, K.M.; Durand, M.; Alsdorf, D.E.; Shum, C.K. Comparing satellite derived precipitation datasets using the Hillslope River Routing (HRR) model in the Congo River Basin. *Hydrol. Process.* **2011**, *25*, 3216–3229.
7. Lee, H.; Beighley, R.E.; Alsdorf, D.; Jung, H.C.; Shum, C.K.; Duan, J.; Guo, J.; Yamazaki, D.; Andreadis, K. Characterization of terrestrial water dynamics in the Congo Basin using GRACE and satellite radar altimetry. *Remote Sens. Environ.* **2011**, *115*, 3530–3538.
8. Alsdorf, D.E.; Smith, L.C.; Melack, J.M. Amazon floodplain water level changes measured with interferometric SIR-C radar. *IEEE Trans. Geosci. Remote Sens.* **2001**, *39*, 423–431.
9. Alsdorf, D.; Bates, P.; Melack, J.; Wilson, M.; Dunne, T. Spatial and temporal complexity of the Amazon flood measured from space. *Geophys. Res. Lett.* **2007**, *34*, 1–5.
10. Wdowinski, S.; Kim, S.W.; Amelung, F.; Dixon, T.H.; Miralles-Wilhelm, F.; Sonenshein, R. Space-based detection of wetlands' surface water level changes from L-band SAR interferometry. *Remote Sens. Environ.* **2008**, *112*, 681–696.
11. Lu, Z.; Kwoun, O.I. Radarsat-1 and ERS InSAR analysis over southeastern coastal Louisiana: Implications for mapping water-level changes beneath swamp forests. *IEEE Trans. Geosci. Remote Sens.* **2008**, *46*, 2167–2184.
12. Chul Jung, H.; Alsdorf, D. Repeat-pass multi-temporal interferometric SAR coherence variations with Amazon floodplain and lake habitats. *Int. J. Remote Sens.* **2010**, *31*, 881–901.
13. Kim, S.W.; Hong, S.H.; Won, J.S. An application of L-band synthetic aperture radar to tide height measurement. *IEEE Trans. Geosci. Remote Sens.* **2005**, *43*, 1472–1478.
14. Kim, J.W.; Lu, Z.; Lee, H.; Shum, C.K.; Swarzenski, C.M.; Doyle, T.W.; Baek, S.H. Integrated analysis of PALSAR/Radarsat-1 InSAR and ENVISAT altimeter data for mapping of absolute water level changes in Louisiana wetlands. *Remote Sens. Environ.* **2009**, *113*, 2356–2365.
15. Hess, L.L.; Melack, J.M.; Novo, E.M.L.M.; Barbosa, C.C.F.; Gastil, M. Dual-season mapping of wetland inundation and vegetation for the central Amazon basin. *Remote Sens. Environ.* **2003**, *87*, 404–428.
16. Martinez, J.M.; Le Toan, T. Mapping of flood dynamics and spatial distribution of vegetation in the Amazon floodplain using multitemporal SAR data. *Remote Sens. Environ.* **2007**, *108*, 209–223.
17. Kasischke, E.S.; Smith, K.B.; Bourgeau-Chavez, L.L.; Romanowicz, E.A.; Brunzell, S.; Richardson, C.J. Effects of seasonal hydrologic patterns in south Florida wetlands on radar backscatter measured from ERS-2 SAR imagery. *Remote Sens. Environ.* **2003**, *88*, 423–441.
18. Grings, F.M.; Ferrazzoli, P.; Jacobo-Berlles, J.C.; Karszenbaum, H.; Tiffenberg, J.; Pratolongo, P.; Kandus, P. Monitoring flood condition in marshes using EM models and Envisat ASAR observations. *IEEE Trans. Geosci. Remote Sens.* **2006**, *44*, 936–941.
19. Grings, F.M.; Ferrazzoli, P.; Karszenbaum, H.; Salvia, M.; Kandus, P.; Jacobo-Berlles, J.C.; Perna, P. Model investigation about the potential of C band SAR in herbaceous wetlands flood monitoring. *Int. J. Remote Sens.* **2008**, *29*, 5361–5372.

20. Trung, V.N.; Choi, J.H.; Won, J.S. A land cover variation model of water level for the floodplain of Tonle Sap, Cambodia, derived from ALOS PALSAR and MODIS data. *IEEE J. Sel. Top Appl. Earth Obs. Remote Sens.* **2013**, *6*, 2238–2253.
21. Kim, J.-W.; Lu, Z.; Jones, J.W.; Shum, C.K.; Lee, H.; Jia, Y. Monitoring everglades freshwater marsh water level using L-band synthetic aperture radar backscatter. *Remote Sens. Environ.* **2014**, *150*, 66–81.
22. Lee, H.; Shum, C.K.; Yi, Y.; Ibaraki, M.; Kim, J.-W.; Braun, A.; Kuo, C.-Y.; Lu, Z. Louisiana wetland water level monitoring using retracked TOPEX/POSEIDON altimetry. *Mar. Geod.* **2009**, *32*, 284–302.
23. Birkett, C.M.; Mertes, L.A.K.; Dunne, T.; Costa, M.H.; Jasinski, M.J. Surface water dynamics in the Amazon Basin: Application of satellite radar altimetry. *J. Geophys. Res.: Atmos.* **2002**, *107*, LBA 26-1–LBA 26-21.
24. Lee, H.; Jung, H.C.; Yuan, T.; Beighley, R.E.; Duan, J. Controls of terrestrial water storage changes over the central Congo Basin determined by integrating PALSAR ScanSAR, Envisat altimetry, and GRACE data. In *Remote Sensing of the Terrestrial Water Cycle*; John Wiley & Sons, Inc: Hoboken, NJ, USA, 2014; pp. 115–129.
25. Hansen, M.C.; DeFries, R.S.; Townshend, J.R.G.; Carroll, M.; Dimiceli, C.; Sohlberg, R.A. Global percent tree cover at a spatial resolution of 500 meters: First results of the MODIS vegetation continuous fields algorithm. *Earth Interact.* **2003**, *7*, 1–15.
26. DiMiceli, C.M.; Carroll, M.L.; Sohlberg, R.A.; Huang, C.; Hansen, M.C.; Townshend, J.R.G. *Annual Global Automated MODIS Vegetation Continuous Fields (MOD44B) at 250 m Spatial Resolution for Data Years Beginning Day 65, 2000–2010*; Collection 5 Percent Tree Cover; University of Maryland: College Park, MD, USA, 2010.
27. Bailey, R.G.; Banister, K.E. The Zaïre River system. In *The Ecology of River Systems*; Davies, B.R.,Walker, K.F., Eds.; Springer Netherlands: Dordrecht, The Netherlands, 1986; Volume 60, pp. 201–224.
28. Thieme, M.L.; Abell, R.; Burgess, N.; Lehner, B.; Dinerstein, E.; Olson, D. *Freshwater Ecoregions of Africa and Madagascar: A Conservation Assessment*; Island Press: Washington, DC, USA, 2005.
29. Baugh, C.A.; Bates, P.D.; Schumann, G.; Trigg, M.A. SRTM vegetation removal and hydrodynamic modeling accuracy. *Water Resour. Res.* **2013**, *49*, 5276–5289.
30. Brown, C.G.; Sarabandi, K.; Pierce, L.E. Model-based estimation of forest canopy height in red and Austrian pine stands using shuttle radar topography mission and ancillary data: A proof-of-concept study. *IEEE Trans. Geosci. Remote Sens.* **2010**, *48*, 1105–1118.
31. Tateishi, R.; Uriyangqai, B.; Al-Bilbisi, H.; Ghar, M.A.; Tsend-Ayush, J.; Kobayashi, T.; Kasimu, A.; Hoan, N.T.; Shalaby, A.; Alsaaideh, B.; Enkhzaya, T.; Gegentana; Sato, H.P. Production of global land cover data—GLCNMO. *Int. J. Digit. Earth.* **2010**, *4*, 22–49.
32. Sita, P. Etude préliminaire de la végétation de l'île M'Bamou. Available online: http://horizon.documentation.ird.fr/exl-doc/pleins_textes/divers12-05/12250.pdf (accessed on 20 December 2014).
33. Wingham, D.J.; Rapley, C.G.; Griffiths, H. New techniques in satellite altimeter tracking systems. In *Proceedings of 1986 International Geoscience and Remote Sensing Symposium (IGARSS'86) on Remote Sensing: Today's Solutions for Tomorrow's Information Needs*; ESA Publication Division: Noordwijk, The Netherlands, 1986; Volume 3.

34. Rosenqvist, A.; Shimada, M.; Ito, N.; Watanabe, M. ALOS PALSAR: A pathfinder mission for global-scale monitoring of the environment. *IEEE Trans. Geosci. Remote Sens.* **2007**, *45*, 3307–3316.
35. Pope, K.O.; Rejmankova, E.; Paris, J.F.; Woodruff, R. Detecting seasonal flooding cycles in marshes of the Yucatan Peninsula with SIR-C polarimetric radar imagery. *Remote Sens. Environ.* **1997**, *59*, 157–166.
36. Grings, F.; Salvia, M.; Karszenbaum, H.; Ferrazzoli, P.; Kandus, P.; Perna, P. Exploring the capacity of radar remote sensing to estimate wetland marshes water storage. *J. Environ. Manage.* **2009**, *90*, 2189–2198.
37. Shimada, M.; Isoguchi, O.; Tadono, T.; Isono, K. PALSAR radiometric and geometric calibration. *IEEE Trans. Geosci. Remote Sens.* **2009**, *47*, 3915–3932.
38. Werner, C.; Wegmüller, U.; Strozzi, T.; Wiesmann, A. Gamma SAR and interferometric processing software. In *Proc of ERS-Envisat Symp*; Citeseer: Gothenburg, Sweden, 2000; Volumer 461.
39. NASA Shuttle Radar Topography Mission. Available online: https://lpdaac.usgs.gov/products/measures_products_table/srtmgl1 (accessed on 15 February 2015).
40. Lee, H.; Shum, C.K.; Yi, Y.; Braun, A.; Kuo, C.-Y.Y. Laurentia crustal motion observed using TOPEX/POSEIDON radar altimetry over land. *J. Geodyn.* **2008**, *46*, 182–193.
41. Kruizinga, G.J. Dual-Satellite Altimeter Crossover Measurements for Precise Orbit Determination. Ph.D. Dissertation, University of Texas, Austin, TX, USA, 1997.
42. Wegmuller, U. Automated terrain corrected SAR geocoding. In Proceedings of IEEE 1999 International Geoscience and Remote Sensing Symposium, Hamburg, Germany, 28 June–2 July 1999; Volume 3, pp. 1712–1714.
43. Nelson, M.D.; McRoberts, R.E.; Hansen, M.C. Forest land area estimates from Vegetation Continuous Fields. In Proceedings of Proceedings of the Tenth Biennial Forest Service Remote Sensing Applications Conference—Remote Sensing for Field Users, Salt Lake City, UT, USA, 5–9 April 2004; pp. 5–9.
44. Schmitt, C.B.; Burgess, N.D.; Coad, L.; Belokurov, A.; Besançon, C.; Boisrobert, L.; Campbell, A.; Fish, L.; Gliddon, D.; Humphries, K. Global analysis of the protection status of the world's forests. *Biol. Conserv.* **2009**, *142*, 2122–2130.
45. Hansen, M.C.; Roy, D.P.; Lindquist, E.; Adusei, B.; Justice, C.O.; Altstatt, A. A method for integrating MODIS and Landsat data for systematic monitoring of forest cover and change in the Congo Basin. *Remote Sens. Environ.* **2008**, *112*, 2495–2513.
46. Costa, M.P.F.; Niemann, O.; Novo, E.; Ahern, F. Biophysical properties and mapping of aquatic vegetation during the hydrological cycle of the Amazon floodplain using JERS-1 and Radarsat. *Int. J. Remote Sens.* **2002**, *23*, 1401–1426.
47. Le Toan, T.; Ribbes, F.; Wang, L.-F.; Floury, N.; Ding, K.-H.; Kong, J.A.; Fujita, M.; Kurosu, T. Rice crop mapping and monitoring using ERS-1 data based on experiment and modeling results. *IEEE Trans. Geosci. Remote Sens.* **1997**, *35*, 41–56.
48. Kwoun, O.; Lu, Z. Multi-temporal RADARSAT-1 and ERS backscattering signatures of coastal wetlands in southeastern Louisiana. *Photogramm. Eng. Remote Sens.* **2009**, *75*, 607–617.
49. Alsdorf, D.E.; Rodríguez, E.; Lettenmaier, D.P. Measuring surface water from space. *Rev. Geophys.* **2007**, doi:10.1029/2006RG000197.

50. Wilson, M.D.; Bates, P.; Alsdorf, D.; Forsberg, B.; Horritt, M.; Melack, J.; Frappart, F.; Famiglietti, J. Modeling large-scale inundation of Amazonian seasonally flooded wetlands. *Geophys. Res. Lett.* **2007**, *34*, 4–9.
51. Jung, H.C.; Jasinski, M.; Kim, J.W.; Shum, C.K.; Bates, P.; Neal, J.; Lee, H.; Alsdorf, D. Calibration of two-dimensional floodplain modeling in the central Atchafalaya Basin Floodway System using SAR interferometry. *Water Resour. Res.* **2012**, *48*, 1–13.